Qualitative analysis of the response regimes and triggering mechanism of bistable NES

Zhenhang Wu, Sébastien Seguy, Manuel Paredes

Noname manuscript No.
(will be inserted by the editor)

Qualitative analysis of the response regimes and triggering mechanism of bistable NES

Zhenhang Wu · Sébastien Seguy · Manuel Paredes

Received: date / Accepted: date

Abstract The main focus of this study is the development of an adapted complex variable method in the vicinity of equilibrium in bistable Nonlinear Energy Sink(NES). A simplified chaos trigger model is established to describe the distance between the stable phase cycle and the pseudo-separatrix. An analytical expression can predict the excitation threshold for chaos occurrence. The relative positions between the chaos trigger threshold line and the Slow Invariant Manifold (SIM) structure can express the distribution of response regimes under growing harmonic excitation. The degeneration of the response regimes can be interpreted by the qualitative analysis method, which helps to classify the bistable NES. The experiment confirms the analytical result of intra-well oscillation in the frequency domain. The characteristic response regimes of weak, modest and strong bistable NES are identified by the experimental results.

Keywords Qualitative analysis · Bistable nonlinear energy sink · Slow invariant manifold · Targeted energy transfer · Trigger mechanism
Declarations The authors have no conflicts of interest to declare that are relevant to the content of this article. The authors declare that the data supporting the findings of this study are available within the article. The authors declare that all procedures performed in this study were in accordance with the ethical standards of COPE. This manuscript is only submitted to the journal

Zhenhang Wu
Institut Clément Ader (ICA), CNRS, INSA-ISAE-Mines Albi-UPS, Université de Toulouse, 3 rue Caroline Aigle, Toulouse, 31400, France
Tel.: +07 61 91 90 78
E-mail: zhenhang.wu@insa-toulouse.fr

Sébastien Seguy
sebastien.seguy@insa-toulouse.fr

Manuel Paredes
manuel.paredes@insa-toulouse.fr

'Nonlinear Dynamics'. The authors declare that this study is complete, unsplit and original.

Acknowledgments The authors acknowledge the Chinese Scholarship Council under Grant No. 201801810128 for their financial support.

1 Introduction

The Nonlinear Energy Sink (NES), a novel vibration absorber, has become an active research field in recent decades. It consists of nonlinear component and an attached mass to achieve the vibration mitigation. The traditional Tuned Mass Damper (TMD) has to be tuned to closely match the mechanical system's natural frequency in order to absorb more energy. The performance of a TMD will decline dramatically if the applied excitation frequency shifts. In contrast, the NES possesses a broader range of absorbed frequencies because of its self-adaptive stiffness, and its energy-dependent resonating frequency characteristic [1]. The NES also has some other remarkable advantages: a lighter attached mass, and a capability to wipe out the resonance peak [2].

The most significant properties are that the energy of the Linear Oscillator (LO) is irreversibly transferred into the NES and is rapidly dissipated by the damping [3]. This phenomenon, called Targeted Energy Transfer (TET), is based on 1:1 resonance capture. If the primary system is under harmonic forcing, it gives rise to a beating response, which is referred to as a Strongly Modulated Response (SMR). The appearance of folded singularities in the Slow Invariant Manifold (SIM) implies a necessary excitation threshold condition to activate the SMR [4]. The stability of the SMR is transformed into a 1-D mapping problem. The analytical approach provides a necessary damping condition to ensure SMR [5]. The NES concept has been explored in both numerical [6,7] and experimental ways [8,9].

Various types of NES, such as piecewise NES [10], rotary NES [11], and vibro-impact NES (VI NES) [12,25], have been investigated to better explore the potential of NES. The absorption performance of different configurations among cubic NES and bistable NES shows the priority of the latter NES to reduce the band width of the initial energies input [14,15]. Single-sided VI NES leading to more effective shock mitigation are compared to a double-sided restricted VI NES [16]. The mechanical applications in structural seismic control [17] and in mitigating chatter vibration [18] in the tuning process have been studied.

Nowadays, one of the widely used analytical approaches for processing NES is the complexification averaging (CX-A) method to derive the modulation equation and compute the fixed points [19]. The application of the standard multiple-scales procedure gives a slow/fast partition of the dynamics by introducing a fast time scale τ and a slow timescale $\tau_1 = \epsilon\tau$ [2–7]. However, as for bistable NES, which involves essential chaotic motion, a rigorous theoretical description is not possible. The analytical study presented here provides an adequate description of the initial highly energetic regime of intensive energy

transfer from LO to NES on a reduced system without considering damping and excitation [20]. A study of parameters, based on an approach complexifying the Hamiltonian system, reveals the frequency-energy characteristic of the bistable case. The backbone of periodic solutions of the conservative system in the frequency–energy plane depicts in-phase (S11+) and out-of-phase (S11–) 1:1 resonance oscillations [21], which are responsible for the intensive energy exchange in Hamiltonian systems.

The classification of bistable NES response regimes is mainly based on empirical observation. In a low energy case, subharmonic resonances and chaotic cross-well oscillations are excited. In a higher energy case, the fundamental (1:1) and subharmonic (1:3) resonances mainly govern the dynamic behaviour. In [22], an extension of Manevitch's complex variables shows that it is potentially better to describe higher harmonics in an initial high energy input. If the bistable NES system is under harmonic excitation input, four typical response regimes at different energy levels appear in turn: (1) intra-well oscillation, (2) chaotic inter-well oscillation, (3) strongly modulated response, (4) steady-state [23]. The optimal point occurs in the transition from the SMR stage to a stable response. Adjusting a variable pitch spring can provide the desired nonlinear stiffness with the optimal design [25]. The robustness of optimal design is verified in [16], which also concludes that the damping condition mainly determines the ceiling of maximum efficiency in the optimal cubic NES.

To construct and extend flexible use of bistable NES in different mechanical contexts, several materials have been tested, e.g., cantilever beam [26], magnetic material [27,28], bistable thin plate [29], spring system [23,30], and buckled beam[31].

This work is organised as follows. In Section 2, an adapted complex variable is developed to predict the excitation threshold for chaos to occur. Section 3 proposes a simplified trigger chaos model and verifies it numerically. In Section 4, the relative position of the chaos trigger line and its global SIM structure express an alternating phenomenon of response regimes and, in Section 5, the experimental result verifies the analytical intra-well result calculated using the adapted complex variables method. Section 6 investigates the frequency distribution of three negative stiffness cases from the previous section. The last section mentions some noteworthy conclusions.

2 Adapted complex variables method

Intra-well oscillation relates to a low energy motion that is restricted to one of the potential wells. It will become chaotic with increasing energy. An exact method to describe the intra-well oscillation is necessary to divide the regimes.

First of all, the target system consists of a Linear Oscillator (LO) m_1, which is sustained by a harmonic excitation $x_e = Gcos(\omega t)$ through linear stiffness k_1 and viscous damping coefficient c_1. A lightweight m_2 is coupled to LO with viscous damping c_2 by means of cubic stiffness k_3 and negative stiffness k_2. The schema of a bistable NES system is presented in Fig. 1.

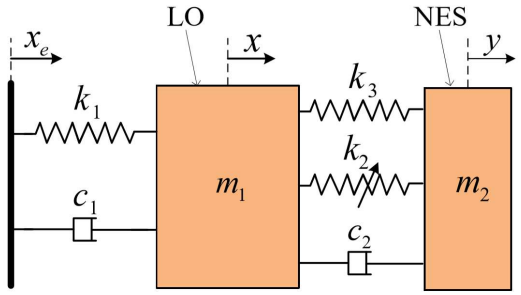

Fig. 1 The schematic of bistable NES system

$$\begin{aligned} &m_1\ddot{x} + k_1x + c_1\dot{x} + c_2(\dot{x}-\dot{y}) + k_2(x-y)^3 + k_3(x-y) = k_1x_e + c_1\dot{x}_e \\ &m_2\ddot{y} + c_2(\dot{y}-\dot{x}) + k_2(y-x)^3 + k_3(y-x) = 0 \end{aligned} \tag{1}$$

The governing equation (1) can be written in rescaled form (3) by introducing the following rescaled variables (2). The new variable $v = x + \epsilon y$ represents the displacement of mass and $w = x - y$ is the relative displacement of the bistable NES.

$$\begin{aligned} &\epsilon = \tfrac{m_2}{m_1}, \omega_0^2 = \tfrac{k_1}{m_1}, K = \tfrac{k_2}{m_2\omega_0^2}, \delta = \tfrac{k_3}{m_2\omega_0^2} \\ &\lambda_1 = \tfrac{c_1}{m_2\omega_0}, \lambda_2 = \tfrac{c_2}{m_2\omega_0}, F = \tfrac{G}{\epsilon}, \Omega = \tfrac{\omega}{\omega_0}, \tau = \omega_0 t \end{aligned} \tag{2}$$

$$\begin{aligned} &\ddot{v} + \epsilon\lambda_1\tfrac{\dot{v}+\epsilon\dot{w}}{1+\epsilon} + \tfrac{v+\epsilon w}{1+\epsilon} = \epsilon F\cos\Omega\tau \\ &\ddot{w} + \epsilon\lambda_1\tfrac{\dot{v}+\epsilon\dot{w}}{1+\epsilon} + \tfrac{v+\epsilon w}{1+\epsilon} + \lambda_2(1+\epsilon)\dot{w} + K(1+\epsilon)w^3 + \delta(1+\epsilon)w = \epsilon F\cos\Omega t \end{aligned} \tag{3}$$

The system is investigated in the vicinity of 1:1 resonance where LO and NES oscillate at the identical frequency Ω. The traditional treatment of w defines it as the relative distance between LO and NES. However, the negative stiffness generates one equilibrium on either side of the origin of the coordinates. The small oscillation around equilibria will be described as a large amplitude with respect to $w = 0$. It also generates a massive error in the traditional analytical calculation of NES amplitude. It is necessary to consider the position of equilibrium and define the distance between the NES and the equilibrium point as a relative displacement.

So, two adapted complex variables describing the neighbourhood of positive stable equilibrium point $x_0 = \sqrt{-\delta/K}$ are given by

$$\begin{aligned} \phi_1(\tau)e^{i\Omega\tau} &= \tfrac{d}{d\tau}v(\tau) + i\Omega(v(\tau) + \epsilon x_0) \\ \phi_2(\tau)e^{i\Omega\tau} &= \tfrac{d}{d\tau}w(\tau) + i\Omega(w(\tau) - x_0) \end{aligned} \tag{4}$$

where $i = \sqrt{-1}$ the imaginary unit. A minus sign should be added in (4) in order to study the local dynamics near the negative stable equilibrium $-x_0$.

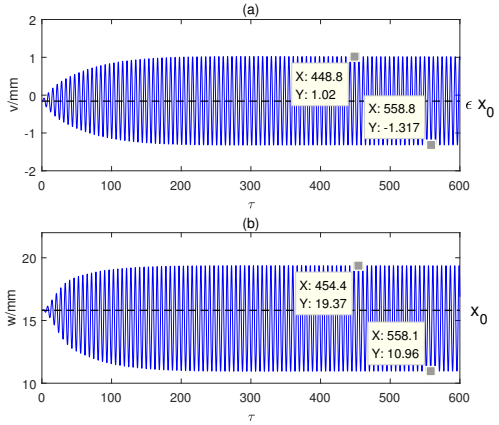

Fig. 2 Time displacement of (a) LO and (b) NES in an intra-well oscillation stage, with the excitation amplitude G = 0.05mm,σ = 0, initial condition $\dot{w}(0) = \dot{v}(0) = 0$,$w(0) = x_0, v(0) = -\epsilon x_0$, with system parameters: ϵ =0.01, λ_1 =1.67, λ_2=0.167, K =1742, δ =-0.43 and equillibrum position x_0 = 15.8mm

Only intra-well oscillation on the positive side falls within the scope of our present considerations, for the sake of symmetry.

In a potential function which is defined by the $H(w) = \delta w^2/4 + Kw^4/4$, it exists two attrctor points at $w = \pm x_0 = \pm\sqrt{-\delta/K}$, where NES possesses the lowest potential energy and is called potential well. When the NES vibrates symmetrically near the positive equilibrium $w = x_0$ as a center in Fig. 2(a) shows, it is termed as intra-well oscillation.

When the system performs a stable response, the upper displacement position of NES is 19.37mm, and the lower displacement position is 10.96mm. The center of the upper and lower displacement position is 15.17mm, which is close to the position equilibrium point x_0 = 15.8mm. However, the numerical simulation confirms that the amplitude of LO is also slightly asymmetrical as Fig. 2(a) shows. The upper displacement position of LO is 1.02mm and the lower displacement position is -1.317mm. The center of the upper and lower displacement position is -0.15mm, which is negative. The center of LO oscillation approximately locates $-\epsilon x_0$ = -0.158mm. That is the explanation for the different center forms in the (4). By considering the center positions, the ϕ_1 and ϕ_2 can describe better the amplitude of LO and NES with respect to the oscillation centers. Therefore the adapted complex variables assumption fits well the simulation result.

Introducing (4) into (3), and keeping only terms containing $e^{i\Omega\tau}$ yields the following slow modulated system:

$$\begin{array}{l}\dot{\phi}_1+\frac{i\Omega}{2}\phi_1+\frac{\epsilon\lambda_1(\phi_1+\epsilon\phi_2)}{2(1+\epsilon)}-\frac{i(\phi_1+\epsilon\phi_2)}{2\Omega(1+\epsilon)}-\frac{\epsilon F}{2}=0\\ \dot{\phi}_2+\frac{i\Omega}{2}\phi_2+\frac{\epsilon\lambda_1(\phi_1+\epsilon\phi_2)}{2(1+\epsilon)}-\frac{i(\phi_1+\varepsilon\phi_2)}{2\Omega(1+\epsilon)}+\frac{\lambda_2(1+\epsilon)\phi_2}{2}-\frac{3iK(1+\epsilon)\phi_2^2\bar{\phi}_2}{8\Omega^3}\\ -\frac{\epsilon F}{2}-\frac{i\phi_2\delta(1+\epsilon)}{2\Omega}-\frac{3iK(1+\epsilon)\phi_2{x_0}^2}{2\Omega}=0\end{array}\tag{5}$$

where $\overline{\phi}_2$ is the complex conjugate of ϕ_2. The stable response of intra-well oscillation corresponds to the fixed point of (5) when the derivative equals zero. Through an algebraic operation, the analytical amplitude of the system can be expressed in a more convenient form. Coefficients α_i (i = 1..3) are not given here due to their length.

$$\begin{array}{c}\phi_{10}=\frac{\frac{i\epsilon\phi_{20}}{\Omega(1+\varepsilon)}-\frac{\varepsilon^2\lambda_1\phi_{20}}{1+\varepsilon}+\varepsilon F+i\varepsilon^2\lambda_1 F\Omega}{i\Omega+\frac{\varepsilon\lambda_1}{1+\varepsilon}-\frac{i}{\Omega(1+\varepsilon)}}\\ \alpha_3 Z_{20}^3+\alpha_2 Z_{20}^2+\alpha_1 Z_{20}+\alpha_0 F^2=0,\quad Z_{20}=|\phi_{20}|^2\end{array}\tag{6}$$

The stability of intra-well oscillation is studied by introducing a small perturbation ρ_j and its complex conjugate $\overline{\rho_j}, j=1,2$ into the fixed point equation (5).

$$\phi_1=\phi_{10}+\rho_1,\quad \phi_2=\phi_{20}+\rho_2, \overline{\phi_1}=\overline{\phi_{10}}+\overline{\rho_1}, \overline{\phi_2}=\overline{\phi_{20}}+\overline{\rho_2}\tag{7}$$

Extracting the perturbation terms gives the characteristic matrix.

$$\begin{bmatrix}\dot{\rho}_1\\ \dot{\rho}_2\\ \dot{\bar{\rho}}_1\\ \dot{\rho}_2\end{bmatrix}=\begin{bmatrix}M_{11} & \epsilon M_{21} & 0 & 0\\ M_{21} & M_{22} & 0 & M_{24}\\ 0 & 0 & \bar{M}_{11} & \epsilon\bar{M}_{21}\\ 0 & \bar{M}_{24} & \bar{M}_{21} & \bar{M}_{22}\end{bmatrix}\begin{bmatrix}\rho_1\\ \rho_2\\ \bar{\rho}_1\\ \bar{\rho}_2\end{bmatrix}\tag{8}$$

where

$$\begin{cases}M_{11}=-\frac{i(1+\epsilon)}{2}-\frac{\epsilon\lambda_1}{2(1+\epsilon)}+\frac{i}{2(1+\epsilon)(1+\epsilon\sigma)}\\ M_{21}=-\frac{\epsilon\lambda_1}{2(1+\epsilon)}+\frac{i}{2(1+\epsilon)(1+\epsilon\sigma)}\\ M_{22}=\frac{3i(1+\epsilon)K\phi_{20}\bar{\phi}_{20}}{2(1+\epsilon)(1+\epsilon\sigma)}-\frac{\lambda_2(1+\epsilon)}{2}+\frac{i\epsilon}{2(1+\epsilon)(1+\epsilon\sigma)}-\frac{i(1+\epsilon\sigma)}{2}-\frac{\epsilon^2\lambda_1}{2(1+\epsilon)}+\frac{i(1+\epsilon)(3Kx_0^2+\delta)}{2(1+\epsilon\sigma)}\\ M_{24}=\frac{3i(1+\epsilon)K\phi_{20}^2}{8(1+\epsilon\sigma)^3}\end{cases}\tag{9}$$

The small detuning parameter σ is applied to measure how near the excitation frequency is to the natural frequency of LO. It gives $\Omega=1+\epsilon\sigma$. The existence of a root of the characteristic equation with a positive real part implies the instability of periodic intra-well oscillation, and vice versa.

The stability of local equilibrium oscillation is deduced and presented in Fig. 3 in the frequency domain. All blue points mean that all the real roots are located in the left-half complex plane. The motion within the well is naturally stable in our case. The absolute value of ϕ_{20} is lower than the chaos threshold. It ensures that the local dynamics is restricted to within the well. If the value of ϕ_{20} exceeds the chaos threshold, it is beyond the scope of our present section, and results in truncation in the vicinity of the natural frequency in Fig. 3.

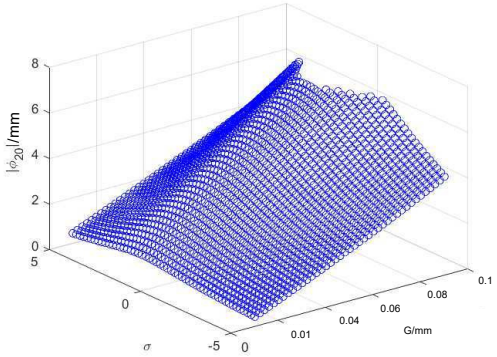

Fig. 3 Amplitude of intra well oscillation in the frequency domain with system parameters: ϵ =0.01, λ_1 =1.67, λ_2=0.167, K =1742, δ =-0.43. Blue points indicate the stability of the solution.

2.1 Asymptotic analysis of local SIM

When considering the adapted variables method, the local SIM structure in which the classical multiple-scales method is applied has to be reconstructed.

$$\begin{gathered}\phi_i = \phi_i\left(\tau_0, \tau_1, \ldots\right), \frac{\mathrm{d}}{\mathrm{d}\tau} = \frac{\partial}{\partial\tau_0} + \epsilon\frac{\partial}{\partial\tau_1} + \epsilon^2\frac{\partial}{\partial\tau_2} + \cdots \\ \tau_k = \epsilon^k\tau, \quad k = 0, 1, \ldots\end{gathered} \tag{10}$$

The dynamic behaviour is considered to involve motion on various times scales. τ_0 represents fast time scales, and $\tau_1 = \epsilon\tau_0$ slow time scales. The rule for derivation under different time scales is presented in (10). By substituting (10) into (9), the terms involving the same power of ϵ, are selected:

$$\begin{gathered}\frac{\partial}{\partial\tau_0}\phi_1 = 0, \\ \frac{\partial}{\partial\tau_0}\phi_2 + \frac{1}{2}\lambda_2\phi_2 + \frac{1}{2}i(\phi_2 - \phi_1) - \frac{1}{2}i\delta\phi_2 - \frac{3}{2}iK\phi_2{x_0}^2 - \frac{3}{8}iK\bar{\phi}_2\phi_2^2 = 0\end{gathered} \tag{11}$$

where the first equation in (11) indicates that the modulation of ϕ_1 is independent of τ_0. Fixed point $\Phi = \lim_{\tau_0\to\infty}\phi_2$ obeys the algebraic equation:

$$\frac{1}{2}\lambda_2\Phi + \frac{1}{2}i(\Phi - \phi_1) - \frac{1}{2}i\delta\Phi - \frac{3}{2}iK\Phi{x_0}^2 - \frac{3}{8}iK\bar{\Phi}\Phi^2 = 0 \tag{12}$$

Taking $\Phi(\tau_1) = N_2e^{i\delta_2}$ and solving the above equation:

$$Z_1 = (\lambda_2^2 + (\delta - 1)\left(\delta - 1 + 6Kx_0^2 + \tfrac{3}{2}KZ_2\right) + 9K^2\left(x_0^2 + \tfrac{Z_2}{4}\right)^2)Z_2 \tag{13}$$

where $Z_1 = |\phi_1|^2, Z_2 = |\Phi|^2$. This structure is deduced by the adapted complex variables method, which is accurate for the intra-well oscillation around the equilibrium point. So this SIM structure is termed as local SIM in comparison with global SIM, which describes the SMR stage or stable periodic stage in a high energy input case. An illustration of the local SIM is given in Fig.4 under

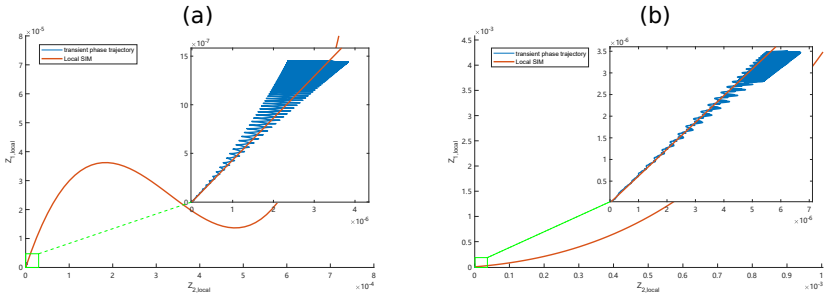

Fig. 4 Local SIM and local phase trajectory for $k_3 = -20$ (δ = -0.174, left), $k_3 = -100$ (δ = -0.871, right). Zoomed insert represents the detailed phase trajectory of intra-well oscillation defined by (6) in the green frame

the different negative stiffnesses where $\epsilon = 0.01, \lambda_1 = 1.67, \lambda_2 = 0.167, K = 1742$.

In a cases of small negative stiffness, the local SIM possesses a characteristic similar to the classic cubic SIM curve, which has singular points like Fig. 4(a). Although most of the local SIM curve is beyond the scope of this application, the zoomed insert part in the vicinity of point (0,0) shows that the phase trajectory climbs along with the SIM. In a more significant negative stiffness case, in Fig. 4(b), the local SIM becomes a monotonically increasing curve. The phase trajectory of the zoomed insert part still oscillates around the SIM, which shows that it is correct for low energy input.

Unlike the traditional description method, e.g. case 1 in Fig. 11, where the phase trajectory has fully separated itself from the SIM, the local SIM describes intra-well motion more accurately. This local SIM structure is developed based on the adapted variable method and its application scope is restricted to an intra-well oscillation. So, the lcoal SIM describes its dynamic behaviours with sufficient accuracy only in a low energy input case. A more significant energy input and cross well oscillation will result in its failure.

2.2 Performance verification

The validity of the adapted complex method can be verified by comparing it with numerical simulations. The difference between amplitudes of w and v calculated by (6). The direct numerical calculation is presented for the various negative stiffness cases ($k_3 = -20$ and $k_3 = -100$) with system parameters: ϵ =0.01, λ_1 =1.67, λ_2=0.167, K =1743, δ =-0.43. These parameters were kept constant in the following numerical simulation.

In a weak negative stiffness case, both LO and NES amplitudes increase with a more intensive excitation amplitude in Fig.5(a),(c). The range of excitation amplitude is selected as [0.005mm, 0.025mm] to ensure that motion of NES is restricted inside the well. In Fig.5(b), the different amplitudes between analytical and numerical results are in a level of $10^{-2}mm$. Meanwhile,

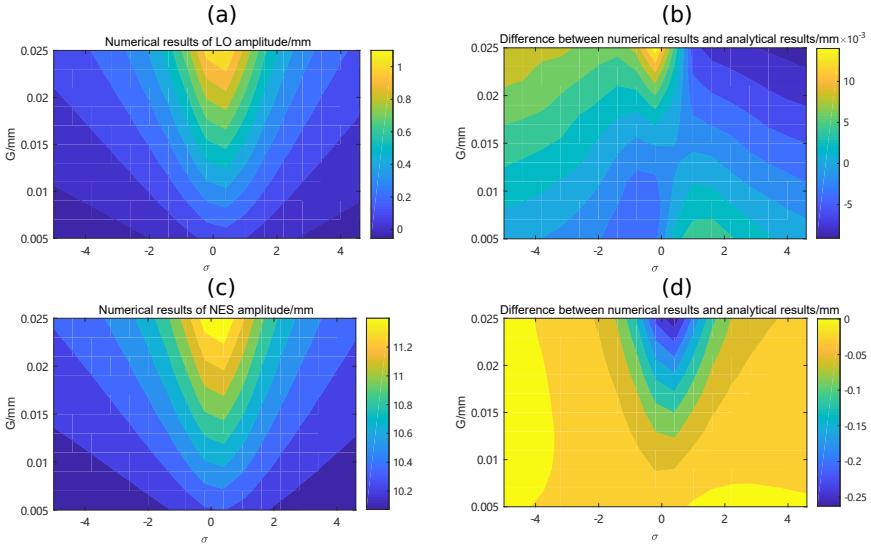

Fig. 5 Comparison of numerical calculations and analytical results of NES. (a), (c) are the numerical amplitudes of NES and LO in a weak negative stiffness case, k_3 = -20. (b), (d) are the relative differences between analytical results and numerical results. Positive values mean numerical result is larger than the analytical result, vice versa

the numerical amplitudes in Fig.5(b) is in a level of 1mm. This difference can be neglected. This indicates that in the case of small negative stiffness, the analytical solution can better describe the amplitude of LO. In Fig.5(b), the analytical NES amplitude is always more significant than the numerical result. The adapted method generates errors mainly in the vicinity of $\sigma = 0$. However, the absolute maximum mistake in NES amplitude calculation is 2.2%, which is still extremely small.

In a more significant negative stiffness case $k_3 = -100$, the deeper potential well requires a more intensive excitation to escape the intra-well oscillation stage. So the amplitude excitation is selected in a larger range [0.005mm, 0.1mm]. In Fig.6(a),(c), the amplitude of NES and LO steady rise with the augment of excitation G. On the negative σ side, both LO and NES amplitudes arrive at their maximums. Analytical LO amplitude results produce a larger value than the numerical results in a high energy input case in In Fig.6(b). In the case of low energy, analytical results of LO amplitude produce lower values than numerical results. As for the analytical results of NES amplitude, it is always smaller than the numerical calculation. The maximal difference occurs in the σ = -1 and G = 0.1mm, where the absolute maximum error is 4%.

Based on the above disscations, the adapted complex method can calculate a fixed point of system in the intra-well oscillation stage. As long as the NES oscillate with respect to the attactor $w = x_0$, NES amplitudes calcucation in Fig.5 and 6 shows its accuracy in frequency domain. As the stiffness increases, the required excitation amplitude to escape the potential well is also

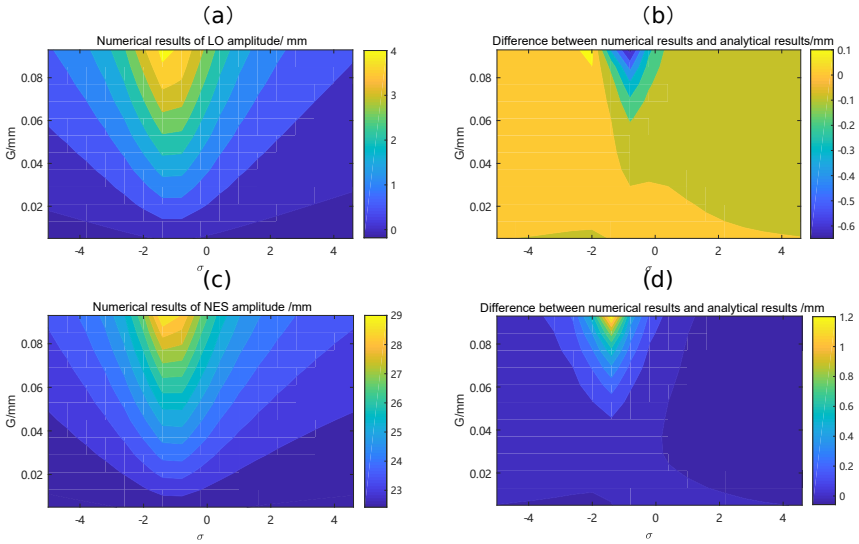

Fig. 6 Comparison of numerical calculations and analytical results of NES. (a), (c) are the numerical amplitudes of NES and LO in a large negative stiffness case, k_3 = - 100. (b), (d) are the relative differences between analytical results and numerical results. Positive values mean numerical result is larger than analtical result, vice versa.

increasing and the application range of complex variables method also extends. Equation. (4) contains the same frequency term Ω, which means both LO and NES oscillate in the same frequency. However, in a high energy input case and higher excitation frequency, 1:3 suhharmonic excitation is activated. The LO oscillates three times faster than the NES. In this case, adapted complex variables method also fails.

3 Analytical prediction of chaotic motion

3.1 Simplified model for chaos occurrence

Chaos always occurs in the transition from intra-well oscillation to inter-well oscillation. The Melnikov method is one of the few effective methods for finding the necessary condition for homoclinic bifurcation and predicting chaotic motion. The transverse intersection of stable and unstable manifold of saddle fixed point and homoclinic bifurcation occurs simultaneously. This kind of global bifurcation is responsible for the prediction of chaotic behaviors.

According to [1], the unperturbed homoclinic orbit of bistable NES that connects the saddle points is shown as the red curves in Fig. 7. Its expression is given by:

$$\begin{aligned} q_+^0(\tau) &= (R \cdot sech(S\tau), -RS \cdot sech(S\tau)\tanh(S\tau)) \\ q_-^0(\tau) &= -q_+^0(\tau) \end{aligned} \tag{14}$$

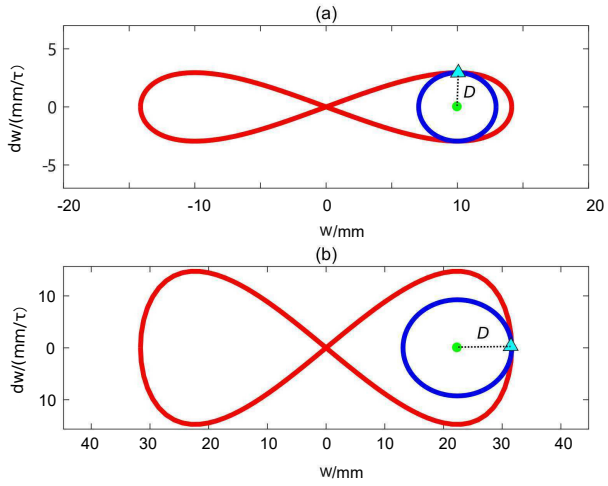

Fig. 7 Different trigger conditions in (a) small negative stiffness value (k_3 = -20N/m, $\delta = -0.174$), (b) large negative stiffness value (k_3 = -100N/m, $\delta = -0.871$). The red line is the pseudo-separatrix, the blue line is the ideal phase trajectory, the green dot is the attractor center $(x_0, 0)$, and the triangle is the contact point. The radius D gives the critical NES amplitude for chaos occurrence.

where $R = \sqrt{-\delta/K}$, $S = \sqrt{-\delta}$. This orbit is also termed as pseudo-separatrix.

The NES oscillates around the attractor (equilibrium) with a small amplitude, and the circle can describe its corresponding stable phase trajectory with sufficient accuracy in the low energy input condition. This stable phase trajectory of intr-well oscillation in damping conditions is similar to the closed homoclinic orbit. When excitation amplitude increases, the phase trajectory expands in a circle with its center at the attractor point $(x_0, 0)$ and the homoclinic orbits break, and phase trajectory touches the separatrix. Its intersection with the pseudo-separatrix can be considered as a symbol of the occurrence of chaos. The different values of δ result in the deformation of geometric shapes of pseudo-separatrix, so the trigger conditions are different, as shown in Fig. 7. The critical δ value divides the trigger conditions into two types: (1) with the contact point located on the pseudo-separatrix or (2) with the contact point located on the extreme right of the pseudo-separatrix.

During the transition from intra-well oscillation to chaotic inter-well oscillation, the phase trajectory will cross the pseudo-separatrix. The trigger condition can be determined by calculating the minimum distance between the point on the pseudo-separatrix and the attractor. The minimal distance D is the minimum radius required for a circle in contact with the pseudo-separatrix, which leads to the critical condition of triggering chaos. The D value, as a function of w, can be defined from (15):

$$D^2 = \left(w - \frac{1}{2}R\sqrt{2}\right)^2 + \frac{S^2 w^2 \left(R^2 - w^2\right)}{R^2} \tag{15}$$

The local minimum distance, which exists only in the following three positions within the interval $[0, R]$, are obtained by taking the derivative of w in the above equation and setting this derivative to zero.

$$w_{1,2,3} = \frac{\left(-\frac{1}{4}\sqrt{2}S + \frac{1}{4}\sqrt{2S^2+8}\right)R}{S}, \frac{R}{\sqrt{2}}, R \tag{16}$$

If the negative stiffness $|\delta|$ exceeds the critical value $(2-\sqrt{2})^2$, (critical negative stiffness k_3 = -39.4 N/m in our case), the minimum distance is always equal to $(1-\frac{\sqrt{2}}{2})R$, which means that the point on the pseudo-separatrix that is closest to the attractor point is always located at the extreme right point, as case (b) in Fig. 7 shows.

In a case of relatively greater negative stiffness, it is reasonable to consider the distance between the extreme right point and the attractor as the critical amplitude. If the final stable NES amplitude $|\phi_{20}|$ exceeds the critical amplitude $|\phi_{20c}| = (1-\frac{\sqrt{2}}{2})R$, chaotic behavior appears. And the amplitudes threshold of NES for chaos occurrence, $Z_a = |\phi_{20c}|^2$ can be expressed in (17).

$$Z_a = \begin{cases} (1-\frac{\sqrt{2}}{2})^2 R^2 & |\delta| > (2-\sqrt{2})^2 \\ \frac{R^2 S^2}{4} & |\delta| \leq (2-\sqrt{2})^2 \end{cases} \tag{17}$$

3.2 Analytical chaos prediction

The assumption is that the intra-well oscillation expands in a circle and intersects the pseudo-separatrix at critical amplitudes $|\phi_{20c}|$ in various negative stiffness cases. If the system's amplitude increases monotonically before its phase trajectory crosses the pseudo separatrix, the trigger condition (17) can be substituted for the stable solution $Z_{20} = Z_a$ and $G_0 c = \epsilon \cdot F$ in the second equation of (6). So the analytical excitation for chaos occurrence is as follows:

$$G_{0c}^2 = -\frac{\epsilon^2 Z_{20}\left(Z_{20}^2\alpha_3 + Z_{20}\alpha_2 + \alpha_1\right)}{\alpha_0} \tag{18}$$

where the α_1, α_2 and α_3 are the same as the coefficients in (6), which are determined by the system parameters. A more exact threshold value of excitation calculated by (18) can be compared with the numerical Lyapunov exponents method in Fig. 9.

the Lyapunov exponent (LE) can be used to quantitatively evaluate chaos behaviors through calculating the average exponential growth or decay of nearby orbits [33]. The definition of the Lyapunov exponent (λ_{LE}) is given:

$$\lambda_{\mathrm{LE}} = \lim_{d(0)\to 0, t\to\infty} \frac{1}{t} \ln\left(\frac{d(t)}{d(0)}\right) \tag{19}$$

where $d(t)$ is the distance in phase space between a given orbit and a test orbit, initially starting infinitesimally close with initial distance $d(0)$. For a periodic solution (orbit), λ_{LE} reduces to be negative when the calculation time

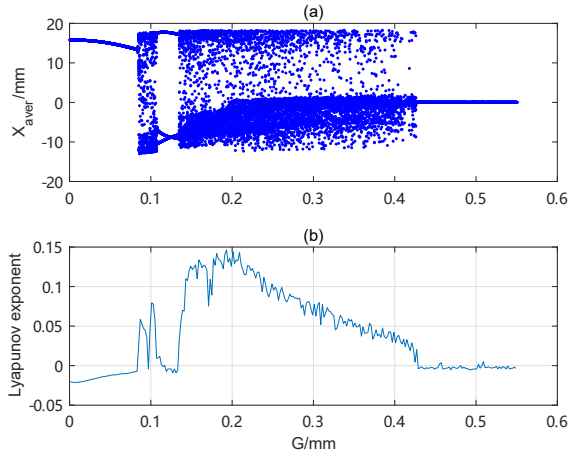

Fig. 8 (a) Bifurcation of bistable NES (k_3 = -50, δ = -0.44) response under variety of excitation amplitude G, X_{aver} means the average distance of NES with respect to the w = 0 position (b) Lyapunov exponent calculation for variety of excitation amplitude G with condition: $\epsilon = 0.01$, $\lambda_1 = 1.67$, $\lambda_2 = 0.167$, K = 1742, $\sigma = 0$

tends to be infinity. As for a chaotic solution, the Lyapunov characteristic exponents approaches a positive value as time increases. Further on, only the maximal component should be considered as an indication of chaos. For a given ordinary differential equation, Wolf created a toolbox in Matlab to calculate LEs, where the algorithm employed for determining the exponent was proposed [35] with a MATLAB implementation found on [36]. So the calculation of Lyapunov exponent is numerically determined from (3). To obesever the validation of Lyapunov method and to inverstigate the excitation amplitude threshold of chaos occurance, the bifurcation diagram under various excitation amplitudes is presented in Fig.8.

Through the Fig. 8. Before excitation amplitude increases to 0.085 mm, the system performs a stable intra-well oscillation, the Lyapunov exponent is negative. Once excitation exceeds the chaos threshold, the exponent turns out to be positive immediately. Even in the 1: 3 subharmonic stage, the Lyapunov exponent appears to be negative again in the range of [0.11mm, 0.14mm]. During the SMR stage (G = [0.2mm, 0.43mm]), chaos motion is mixed with 1:1 resonance, so the Lyapunov exponent is always positive with a decreasing tendency. When excitation exceeds the threshold, the response of the system re-turns to be a stable and optimal state. Lyapunov exponent becomes negative again. The Lyapunov method proves to be efficient enough to determine the chaos threshold. So the chaos threshold G_0c for k_3 = -50N/m is selected as 0.085 mm. So the numerical result of chaos threshold in the function of negative stiffness is marked in the red curve in Fig. 9.

The comparison between numerical predictions and analytical predictions reveals a gradual decline in excitation threshold for chaos occurrence as negative stiffness weakens in Fig. 9. The more intense negative stiffness results in

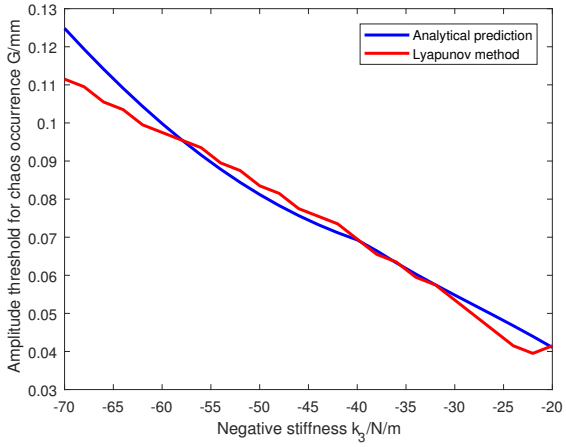

Fig. 9 Comparison of analytical predictions with numerical results of chaos threshold amplitude (harmoinc excitation $\sigma = 0$) under various negative stiffness designs, with condition: $\epsilon = 0.01$, $\lambda_1 = 1.67$, $\lambda_2 = 0.167$, K = 1742

a deeper well requiring more energy input to escape from it, which leads to a higher excitation threshold to trigger chaos.

The analytical prediction values are close to the numerical results for a large range of negative stiffness in Fig. 9. It proves that our analytical method is suitable and accurate enough. According to the performance verification section, the analytical NES amplitude is smaller than the numerical amplitude in the strong negative stiffness case. This implies that the analytical NES amplitude will give a more significant critical trigger excitation.

The accuracy of predictions is changed in strong negative stiffness. The simplified model is less accurate if the phase trajectory is far away from the attractor. At the moment when a trajectory passes the pseudo separatrix, it is always at some distance from the attractor. This distance rises as the value of $|\delta|$ increases.

From another point of view, the adapted complex variables method is based on the stable periodic solution triggering chaos. In a case of much higher negative stiffness, the instantaneous amplitude of the NES exceeds its final stable amplitude, which is inconsistent with the initial assumption that it is the final stable phase trajectory (final periodic solution), rather than the instantaneous amplitude, that triggers the pseudo-separatrix.

In addition, only one side attractor is under consideration. A greater negative stiffness makes the phase trajectory deviate from the ideal circle model. When the phase trajectory passes the mid point between the origin point and the attractor, the other side attractor in the negative side will increase NES amplitude. The asymmetry of amplitude with respect to the attractor renders the prediction results invalid. In the vicinity of the pseudo-separatrix, the intra-well and inter-well subharmonic oscillations are beyond the descriptive

capabilities of the adapted complex variables method. The above potential interpretation explains the generation of error in the process of application of the adapted complex variables method in the prediction of chaos.

4 Qualitative analysis of response regimes

The presentation of negative stiffness introduces chaotic motion essentially changing the response regimes. Two main characteristics are discussed below to interpret the response regimes in various negative stiffness cases.

First, the pseudo-separatrix governs the low energy behaviours and distinguishes them from chaotic motion. Low energy restricts the NES to oscillation around the attractor $(\sqrt{-\delta/K}, 0)$, and expands in one well with growing energy. If the amplitude of w exceeds the extreme right point $(\sqrt{-2\delta/K}, 0)$ of the separatrix, the inter-well chaotic motion pervades two wells and their vicinity.

Secondly, the global SIM branch can better describe the high energy behaviours of bistable NES. The phase trajectory oscillates around the right branch of the global SIM when the system shows SMR or stable response. By applying the classic complex variables $\phi_1 e^{i\Omega\tau} = \dot{v} + i\Omega v, \quad \phi_2 e^{i\Omega\tau} = \dot{w} + i\Omega w$ and a multiple-scales method, the traditional global SIM can be extracted as in (20).

$$\begin{aligned} &Z_1 = \lambda_2^2 Z_2 + (\delta - 1)^2 Z_2 + \tfrac{3K}{2}(\delta - 1) Z_2^2 + \tfrac{9K^2}{16} Z_2^3 \\ &Z_1 = N_1^2, \quad Z_2 = N_2^2 \end{aligned} \tag{20}$$

This method can be found in various references. The unstable regime is divided by the singular value Z_{2i} in the Z_1 and Z_2 plane:

$$Z_{2,i} = \frac{4\left(2(1-\delta) \mp \sqrt{(1-\delta)^2 - 3\lambda_2^2}\right)}{9K}, i = 1, 2 \tag{21}$$

In the SIM plane, there are four characteristic lines worth to emphasize:

1. Line A
   This attractor line is located in $(Z_2 = -\delta/K)$. The phrase trajectory starts from the attractor line A and oscillates around this axis in the intra-well oscillation stage.
2. Line B
   This chaos threshold line is located in $(Z_2 = -2\delta/K)$. It is deduced from the width of the pseudo-separatrix. Once the phase trajectory crosses this line, there is a high possibility to activate chaos. In other words, chaos occurs when the NES amplitude exceeds $\sqrt{-2\delta/K}$ based on the previous simplified chaos trigger model.
3. Line C
   This singularity line C is located in $(Z_2 = Z_{2,1})$. It divides the classic SIM structure into stable and unstable branches. In the cubic NES case, once the phase trajectory crosses this singularity line, a snap-through motion

occurs. However, in an intensive negative stiffness case, this condition does not ensure the occurrence of the jumping phenomenon.

4. Line D
   This singularity line C is located in ($Z_2 = Z_{2,2}$). If the trajectory reaches line D, it jumps definitively to the right stable branch of the SIM even in a bistable NES with a large $|\delta|$ value.

All the four characteristic lines are parallel to the axis Z_1. So the Z_1, Z_2 plane, is divided into two regions: (1) Chaotic region. It occupies range of $Z_2 = [0\ -2\delta/K]$. When the system performs the chaos, phase trajectory will occupy this range. (2) unstable region. It occupies range of $Z_2 = [Z_{2,1}, Z_{2,2}]$. This region is associated with the jumping phenomenon of phase trajectory. It is a temporary region before the system reaches at its final state.

4.1 Classification of bistable NES

The bistable NES preserves some original features of the cubic NES if a small value of negative stiffness is introduced. The distribution of efficiency under inputs of continually increasing energy is presented in Fig. 12, for a better comprehension of the distribution of the regimes. Its efficiency ratio is defined as follows:

$$\begin{aligned} &E_{LO}(\tau) = \int_{\tau_0}^{\tau} \epsilon\lambda_1 \dot{x}^2 d\tau, E_{NES}(\tau) = \int_{\tau_0}^{\tau} \epsilon\lambda_2 (\dot{x} - \dot{y})^2 d\tau, \\ &r_{NES} = \frac{E_{NES}}{E_{LO}+E_{NES}} \times 100\% \end{aligned} \tag{22}$$

4.1.1 Weak bistable NES

Initially, a small value of negative stiffness k_3 = -20 N/m (δ = -0.17) is introduced in the following simulation. This bistable NES preserves some original features of the cubic NES. Fig. 10 shows that the whole excitation range has five distinct phases. For each phase, the typical behavior of the time domain and its phase trajectory are extracted in Fig. 11. The relative positions of four characteristic lines are demonstrated in Fig. 12.

When the NES maintains an intra-well oscillation, e.g. case 1 in Fig. 11c, this low energy level motion is trapped in one of the wells. Because the NES vibrates in the vicinity of equilibrium, the trajectory is quasi-asymmetric around attractor line A. The adapted complex variables method can describe its behaviors better by the local SIM according to the previous section.

In the second stage of Fig. 11, the chaos motion brings a higher efficiency compared to previous stage. And the maximal amplitude (A_m) and avergae amplitude (A_e) curves separate slightly. Increasing energy input causes the NES amplitude to exceed line B and trigger chaotic motion. However, the small value of δ leads to a significant gap between the chaos threshold line B and singularity line D. The phase trajectory can neither activate SMR nor be attracted to the left global SIM branch, but can only expand and take a position near line B, as in case 2 in Fig. 11c.

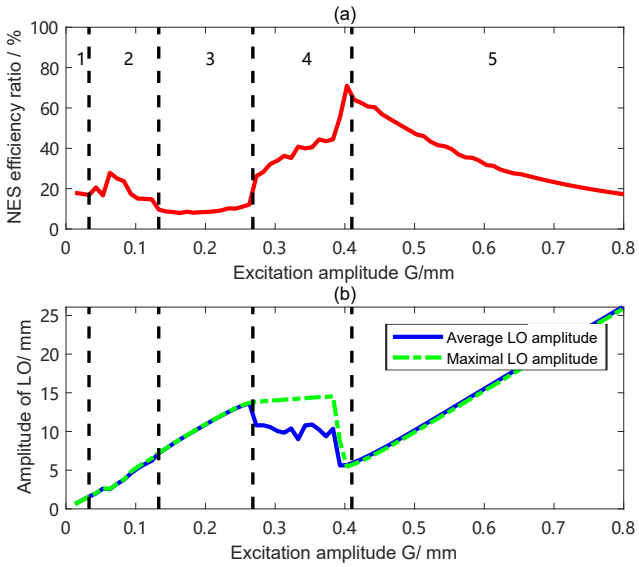

Fig. 10 (a) Energy dissipation ratio of NES (b) maximal and average LO amplitude in weak bistable NES case with k_3 = -20 N/m (δ = -0.17) under harmonic exicitations (σ =0). The blue line represents the average amplitude in a given time interval, the green dashed line is the maximum amplitude. The black dashed lines divide regimes into five stages.

In the third stage of Fig. 10, the LO amplitude increases linearly with increasing G and the corresponding efficiency maintains a low level, which implies that the TET is not activated. After the generation and transient expansion of chaos, the time domain displacement of w is symmetrical to the zero position. The phase trajectory is re-attracted to the left stable global SIM branch as in case 3 in Fig. 11c and rises along the left global SIM branch. This attraction motion that results from the phase trajectory increasing in the Z_1 direction affects the left stable global SIM branch more quickly than the expansion of the phase trajectory in Z_2 direction in the initial low energy input stage.

In the fourth stage of Fig. 10, a complete SMR emerges. TET is activated, so the NES efficiency arises higher. The separation of the maximal amplitude and average amplitude curves manifests an unstable amplitude motion: SMR. The phase trajectory of weak bistable NES moves along with the global SIM structure. However, once the phase trajectory re-enters the chaos region after the efficient energy dissipation, the motion is chaotic in case 4 of Fig. 11, which is different from the cubic NES case.

In the beginning of fifth stage in Fig. 10, the efficiency of NES arrives its maximum. The system achieves an optimal state, whcih is stable and periodic. The maximal efficiency of this weak bistable NES in the Fig. 10 is about 71%. Due to the large amplitude excitaion, the trajectory easily crosses the global SIM unstable region without rising along the left stable branch like case 5

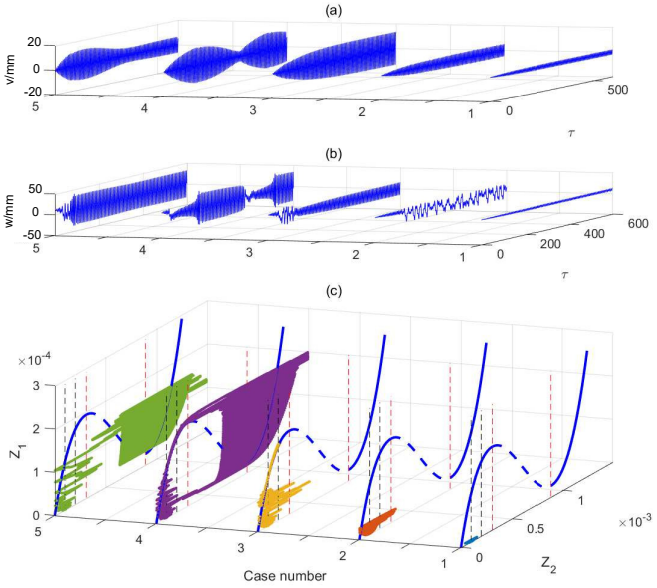

Fig. 11 Response regimes in weak bistable NES with k_3 = -20 N/m (δ = -0.17) (a) v displacement (b) w displacement (c) phase trajectory of Z_2 and Z_1. The 5 typical responses are chosen at various harmonic excitations G = 0.04mm, 0.1mm, 0.25mm, 0.35mm, 0.42mm, with same initial condition ($w(0) = x_0, v(0) = \dot{v}(0) = \dot{w}(0) = 0$), $\sigma = 0$.

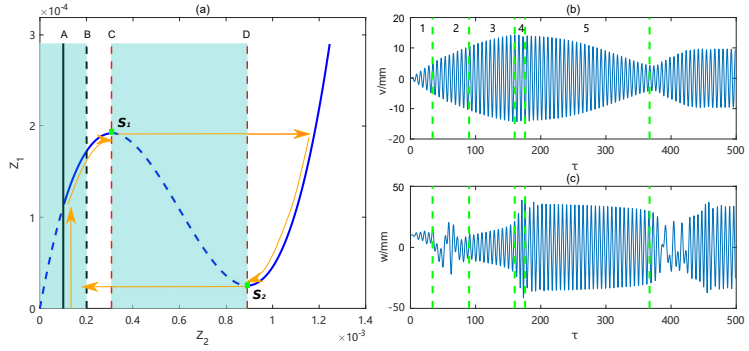

Fig. 12 Characteristic global SIM of weak bistable NES and SMR in the time domain for harmonic exicitation G = 0.35mm, $\sigma = 0$. (a) The global SIM structure with unstable and chaos regions (shaded). Orange arrow line indicates various stages in one SMR cycle. S_1 and S_2 are the singularity points whose locations are defined as $(Z_{2,1}, Z_{1,1})$ and $(Z_{2,2}, Z_{1,2})$. (b) displacement of w, and (c) displacement of v with initial condition ($w(0) = x_0, v(0) = \dot{v}(0) = \dot{w}(0) = 0$). The green lines divide the SMR into various stages corresponding the global SIM explanation by orange arrow line.

of Fig. 11c. Chaos triggers the snap-through motion. The trajectory jumps directly to the right global SIM branch before it crosses the singularity point $S_1 : [Z_{2,1}, Z_{1,1}]$. So the maximal LO amplitude at the jump moment is lower than that of the cubic SMR stage. This implies that the LO can be protected better if there is high energy input in a weak bistable NES case. Since the phase trajectory finally arrives at the right branch of the global SIM without jumping back, it indicates saturation of the capability of absorbing energy. The final position of the phase trajectory will be located in a higher position of the right global SIM branch with an excitation of increasing amplitude. The optimal point ideally occurs at the singularity point $S_2 : [Z_{2,2}, Z_{1,2}]$ in the global SIM structure.

The negative stiffness can not only affect the stage of response regimes, but also influence the SMR behavior. The time domain of SMR, which is divided by green dashed lines in Fig. 12(b) shows five different parts of a complete SMR: (1) intra-well oscillation, (2) chaos expansion, (3) re-attraction to SIM, (4) jumping motion, (5) Targeted Energy Transfer (TET). Compared with the SMR in the pure cubic case, the SMR starts from the intra-well oscillation, so the orange arrow line represents a trajectory rising along line A in Fig. 12(a). The initial motion is constrained in the well and increases until the trajectory is re-attracted to the left stable global SIM branch, on which the orange line converges. As the trajectory crosses the singularity line C, it jumps to the right stable branch of the SIM, and moves down to the other singularity point S_2. 1:1 resonance in this period produces an intense TET and leads to effective dissipation by the NES. Once the NES has dissipated most of the energy of the LO, the phase trajectory of the system jumps back to the chaotic region in the vicinity of attractor line A and waits for the charge of energy under harmonic excitation.

4.1.2 Modest bistable NES

The re-attraction to the global SIM mechanism in a weak bistable system becomes delicate when the $|\delta|$ parameter takes a larger value. The mechanism of this attraction back to the left SIM branch is mainly due to the proximity of the chaos threshold line B to the left global SIM branch. The phase trajectory has a strong possibility of continuing to expand along with line A and being attracted by the left global SIM branch, rather than crossing the unstable region and triggering SMR. If the negative stiffness is intense enough, the chaos trigger line B will be located in the global SIM unstable region. Therefore, the critical condition for the disappearance of re-attraction can be determined as the overlap of line B and line C. The condition is expressed as follows:

$$\begin{aligned} Z_{21} &= \frac{4(2(1-\delta)-\sqrt{(1-\delta)^2-3\lambda_2^2})}{9K} = \frac{-2\delta}{K} \\ \delta_{wm} &= -\frac{8}{7} \pm \frac{2}{7}\sqrt{-7\lambda_2^2+9} \end{aligned} \tag{23}$$

The damping of the NES system determines the critical value of negative stiffness. If the negative critical value exceeds the critical value -0.295 (when

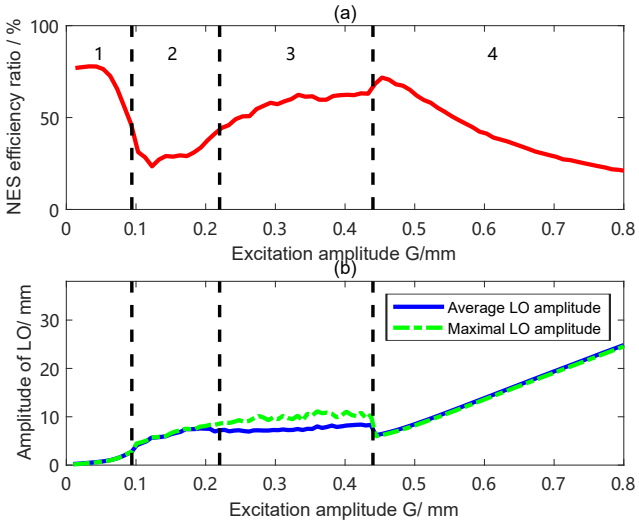

Fig. 13 (a) Energy dissipation ratio of NES (b) maxiaml and average LO amplitude in modest bistable NES case with k_3 = -60N/m (δ = -0.52) under harmonic exicitations (σ =0). The blue line represents the average amplitude in a given time interval, the green dashed line is the maximum amplitude. The black dashed lines divide regimes into four stages.

λ_2= 0.167), the re-attraction to the left global SIM branch mechanism is hardly observable. So it is considered as a modest bistable NES. To better prove this point, the efficiency distribution for a larger negative stiffness case is presented in Fig. 13 with larger negative stiffness case k_3 = -60N/m (δ = -0.52). The efficiency distribution can be divided into 4 stages in Fig. 13 and its characteristic behaviors under inputs of increasing amplitude excitation are presented in Fig. 14.

In the first stage of intra-well oscillation, the NES possesses a high absorbing efficiency. However, as the excitation amplitude increases, its high efficiency is lost and declines drastically.

In the second stage in Fig. 13, chaos emerges. When $|\delta|$ increases, the span and depth of potential well become larger, so a larger amplitude excitation is necessary to trigger the chaotic motion. The critical value is G = 0.09mm, while the chaos threshold excitation is G = 0.03mm in a weak bistable case. This threshold value divides the efficiency distribution figure into the chaotic and intra-well region in Fig. 13, A coexistence of subharmonic oscillations and chaotic motions can be realised in this stage.

In the third stage, SMR occurs in Fig. 13. A greater value of negative stiffness leads to the fact that the chaos trigger line B is located in the global SIM unstable region and is close to the singularity line D in Fig. 15(a),. It can be deduced that SMR is more early to produce in modest bistable case. As already observed in Fig. 13(b), the SMR region starts at G = 0.22mm, which is lower than the SMR trigger excitation G = 0.26mm in weak bistable NES.

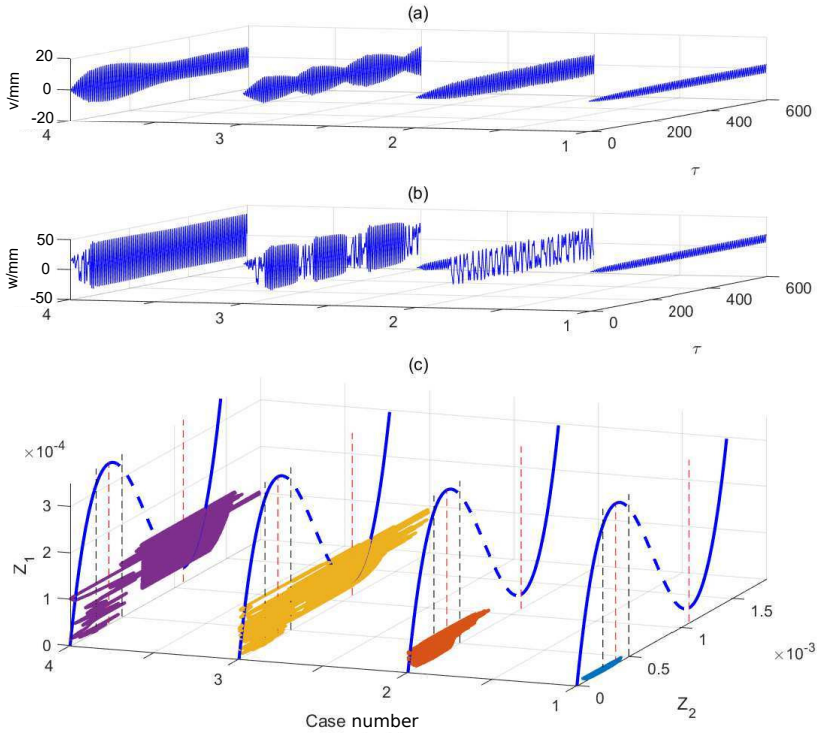

Fig. 14 Response regimes in modest bistable NES with k_3 = -60N/m (δ = -0.52) (a) v displacement (b) w displacement (c) phase trajectory of Z_2 and Z_1. The 4 typical responses are chosen at various harmonic excitations G = 0.08mm, 0.15mm, 0.34mm, 0.45mm, with same initial condition ($w(0) = x_0, v(0) = \dot{v}(0) = \dot{w}(0) = 0$), $\sigma = 0$.

In the fourth stage, the NES system possesses a stable regime again in Fig. 13. The optimal point is generated in this stage. The absorption efficiency of the NES system decreases with increasing external excitation. The maximal efficiency of this modest bistable NES in the Fig. 13 is about 72.5%.

The influence of the more significant value of $|\delta|$ on the global SIM and SMR in the time domain is illustrated in Fig. 15(a). The chaotic region will even overlap the global SIM unstable region partially or entirely if the negative stiffness is increasing. The size of the overlapping parts of the two areas determines the division of the response regimes.

Only four stages have been retained in Fig. 15(b), 15c: (1) intra-well oscillation, (2) chaos expansion, (3) jumping motion, (4) TET. For an SMR cycle of the modest bistable case, the re-attraction to the global SIM part has been completely compressed and replaced by the chaos expansion.

Because the extreme right point in phase trajectory of case 2 is close to singularity line D in Fig. 15c, the SMR is trigged by crossing chaotic region

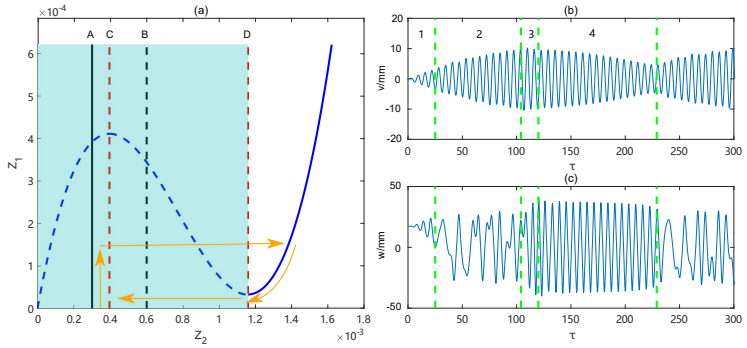

Fig. 15 Characteristic modest bistable global SIM and SMR in the time domain for harmonic excitation G = 0.34 mm, $\sigma = 0$. (a) The global SIM structure with the unstable and chaos regions (shaded). The orange arrow line indicates various stages in one SMR cycle. (b) displacement of w, (c) displacement of v, with initial condition $(w(0) = x_0, v(0) = \dot{v}(0) = \dot{w}(0) = 0)$. The green lines divide the SMR into various stages corresponding to the global SIM explanation by the orange arrow line.

and unstable global SIM region in Z_1, Z_2 plane instead of reaching at the singularity point $(S_1 : [Z_{2,1}, Z_{1,1}])$ and then jumping. It means that the system does not require fully charging the energy to activate SMR. A lower trigger excitation amplitude results in a lower initial Z_1 amplitude, from which the trajectory moves down along the right stable global SIM branch. This shorter path helps NES dissipate energy around the optimal point within a shorter time and higher efficiency. As the case 3 in Fig. 14c, the system performs 3 SMR cycles within 600 τ. However, the weak bistable case performs only one complete SMR during the same time. Chaos provides a much faster way to charge and trigger SMR and accelerate every SMR circle. More SMRs in a fixed time interval are observed in Fig. 14c. That is why the SMR stage in the modest bistable NES has higher efficiency than that of weak bistable NES. A more efficient way to dissipate energy is generated.

4.1.3 Strong bistable NES

The chaos threshold line B will approach the SMR boundary line D more closely for higher negative stiffness. The critical condition is defined as singularity line C is overlap with attractor line A to ensure the close distance between line B and D in global SIM structure.

$$\begin{aligned} Z_{2,1} &= \frac{4}{9}\frac{2-2\delta-\sqrt{(1-\delta)^2-3\lambda_2^2}}{K} = -\frac{\delta}{K} \\ \delta_{ms} &= -\frac{8}{5} - \frac{4}{5}\sqrt{5\lambda_2^2+9} \end{aligned} \tag{24}$$

In the condition of $\lambda_2 = 0.167$, the critical δ value that classifies the modest NES and strong NES is -0.82.

A larger negative stiffness case with $k_3 = 150$ N/m (δ = -1.3) is selected in the strong bistable NES simulation. The expansion of the chaos regime

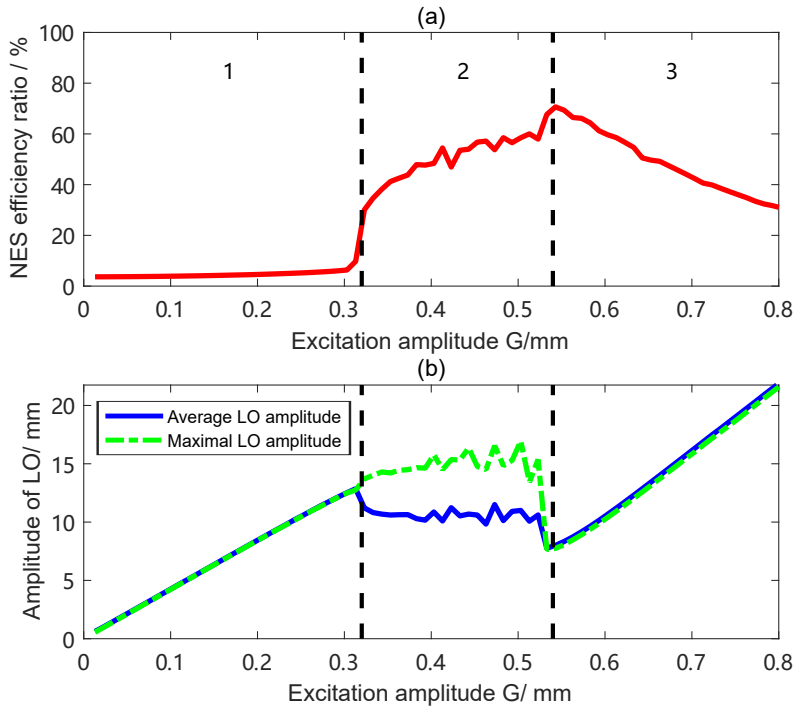

Fig. 16 (a) Energy dissipation ratio of NES (b) maximal and average LO amplitude in strong bistable NES case under harmonic exicitations (σ =0). The blue line represents the average amplitude in a given time interval, the green dashed line is the maximum amplitude. The black dashed lines divide regimes into three stages.

will disappear in effeciency distribution Fig. 16. The trajectory will cross the singularity line D and directly start to jump and perform an SMR. Case 2 in Fig. 17 shows that the snap-through phenomenon occurs at the instant when phase trajectory crosses the chaos region, if the distance between lines B and D is small enough in Fig. 18(a). The energy dissipation ratio can be classified into 3 stages: (1) intra-well oscillation, (2) SMR, (3) stable stage.

In the first intra-well stage, the NES system possesses a low efficiency. It implies that the negative stiffness must be tuned to a modest bistable configuration in order to maintain high efficiency even at low energy input. Too large or too small a negative stiffness will lead to a decrease in efficiency. The energy is mainly localized in the LO, the amplitude of which mainly increases linearly in Fig. 16(b).

In the second SMR stage, the maximal amplitude and average amplitude curves separate drastically in a large distance. Meanwhile, in the modest NES case, both curves separate gradually. It implies that chaos motion is not involved in the SMR stage. It makes the SMR stage of strong bistable NES performs similar to an SMR stage of cubic NES, where the chaos can be hardly

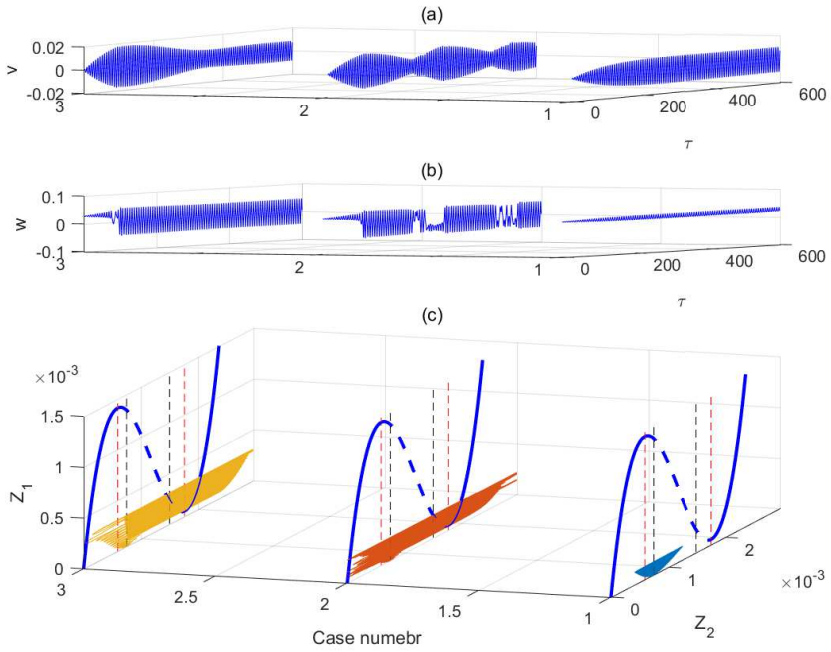

Fig. 17 Response regimes in strong bistable NES with k_3 = 150 N/m (δ = -1.3) (a) v displacement (b) w displacement (c) phase trajectory of Z_2 and Z_1. The 3 typical responses are chosen at various harmonic excitations G = 0.25mm, 0.45mm, 0.55mm, with same initial condition $(w(0) = x_0, v(0) = \dot{v}(0) = \dot{w}(0) = 0)$, $\sigma = 0$

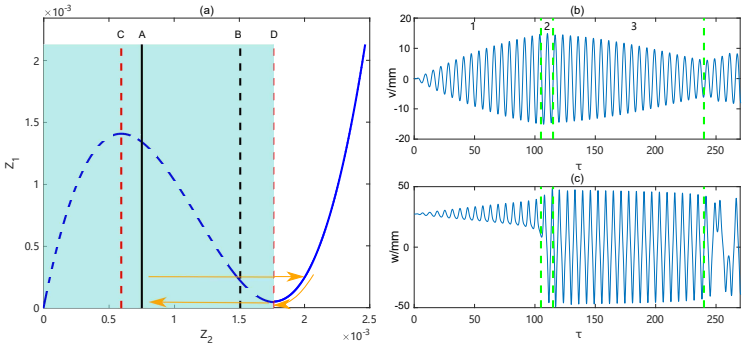

Fig. 18 Characteristic strong bistable global SIM and SMR in the time domain for harmonic excitation G = 0.45mm, $\sigma = 0$. (a) The global SIM structure with the unstable and chaos region (shaded). The orange arrow line indicates various stages in one SMR cycle. (b) displacement of w, (c) displacement of v, with initial condition $(w(0) = x_0, v(0) = \dot{v}(0) = \dot{w}(0) = 0)$. The green lines divide the SMR into various stages corresponding to the global SIM explanation indicated by the orange arrow line

observed. Compared with the SMR stage in weak bistable NES case, the duration of energy pumping in Fig. 17(b) is longer and it has a less absorbing cycle within the same time interval.

In the third stable periodic response stage, the large negative stiffness value increases the excitation amplitude threshold for SMR disappearance, about G = 0.54mm. Meanwhile, the excitation amplitude thresholds for SMR disappearance are G = 0.44mm and G =0.4mm in the modest and weak bistable NES design, respectively. A high $|\delta|$ value can help the system to achieve an optimal state in a higher energy input case. The attractor line A restricts the motion inside of potential well before it jumps out. The maximal efficiency of this strong bistable NES in the Fig. 16 is about 70.5%.

In the strong bistable NES case, the increasing $|\delta|$ results in a simpler form of SMR. The motion of SMR is either in a potential well or in the right stable global SIM branch. The chaotic motion becomes weak and transient. Only 3 parts: (1) intra-well oscillation, (2) snap-through, and (3) TET are classified as in Fig. 18(b), 18c. In the second SMR stage, once the phase trajectory crosses the chaos trigger line B, the right stable branch of the global SIM attracts the phase trajectory.

4.1.4 Abnormal bistable NES

If the negative stiffness is extremely large, another critical condition can be achieved, where the chaos threshold line B coincides with the singularity line D, and the following equation can be derived:

$$\begin{array}{l} \frac{4}{9}\frac{2-2\delta+\sqrt{(1-\delta)^2-3\lambda_2^2}}{K} = -\frac{2\delta}{K} \\ \delta_{wm2} = -\frac{8}{7} \pm \frac{2}{7}\sqrt{-7\lambda_2^2+9} \end{array} \tag{25}$$

Solving the above equation gives a critical negative stiffness of δ_{sa} = -2, above which, bistable NES is classified as an abnormal case. In this abnormal case, the simulation of negative stiffness case k_3 = -250 (δ = -2.2) is carried out.

In this case, the trajectory exceeds the chaos threshold and becomes a stable inter-well oscillation. Because the interaction of chaos threshold line B and the right global SIM branch, the SMR vanishes. Only two regimes persist in the efficiency distribution and LO amplitude in Fig. 21 : (1) intra-well oscillation, and (2) stable periodic response. In contrast to the previous model, the SMR stage is compressed and vanishes, leading to a so-called abnormal bistable NES.

The trigger chaos line B has exceeded on the right side of singularity line D, so the optimal point (maximum efficiency) is not lying on the singular point S_2. The maximal efficiency that an abnormal NES can achieve is much lower than in previous cases, about 50%.

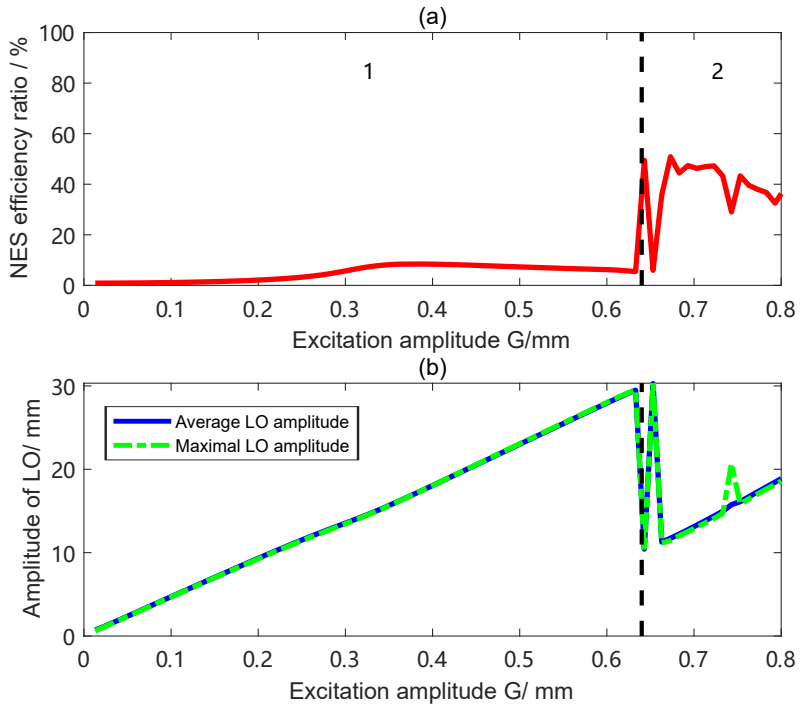

Fig. 19 (a) Energy dissipation ratio of NES (b) maximal and average LO amplitude in abnormal bistable NES case under harmonic exicitations ($\sigma = 0$). The blue line represents the average amplitude, the green dashed line is the maximum amplitude. The black dashed lines divide regimes into two stages.

5 Experimental validation

The first goal of the experimental tests was to verify the feasibility of the intra-well adapted complex variables method in the frequency domain. The second objective was to observe the characteristic response regimes of different bistable NES design under increasing excitation amplitude inputs. Various negative stiffnesses were constructed by adjusting the pre-compression length of the linear spring in the bistable NES. A diagram of the bistable NES and the actual experimental device are presented in Fig. 22 and 23.

The bistable stiffness is constructed by combining 2 linear springs and 2 conical springs that mainly provide the nonlinear stiffness. The conical spring presents two phases: (a) linear phase, (b) nonlinear phase during the compression [14]. When the coils of a conical spring come into contact with each other due to compression, a transition moment occurs that divides the linear and nonlinear phases. So the two conical springs are pre-compressed at the transition point to eliminate the linear phase, as in (a) of Fig. 22. The two linear springs, whose role is to counterbalance the linear stiffness in the nonlinear

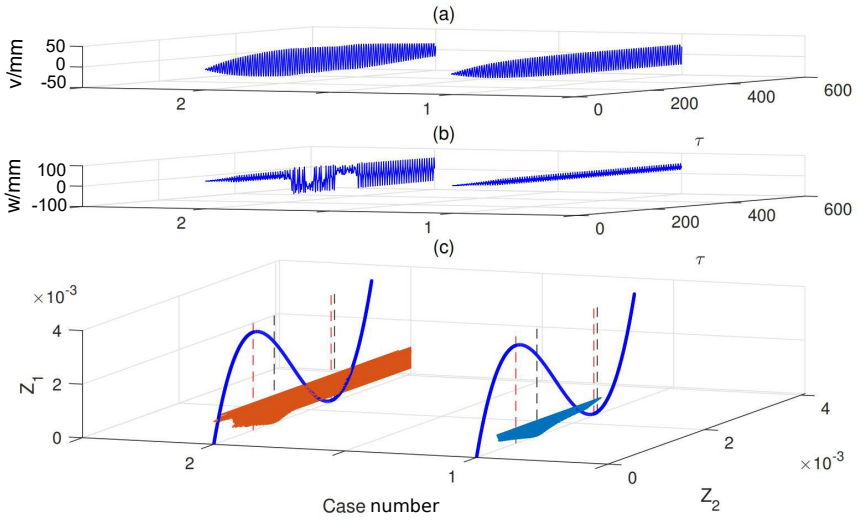

Fig. 20 Response regimes in abnormal bistable NES with k_3 = -250 (δ = -2.2) (a) v displacement, (b) w displacement, (c) phase trajectory of Z_2 and Z_1. The 2 typical responses are chosen at various harmonic excitations G = 0.5mm, 0.7mm, σ = 0.

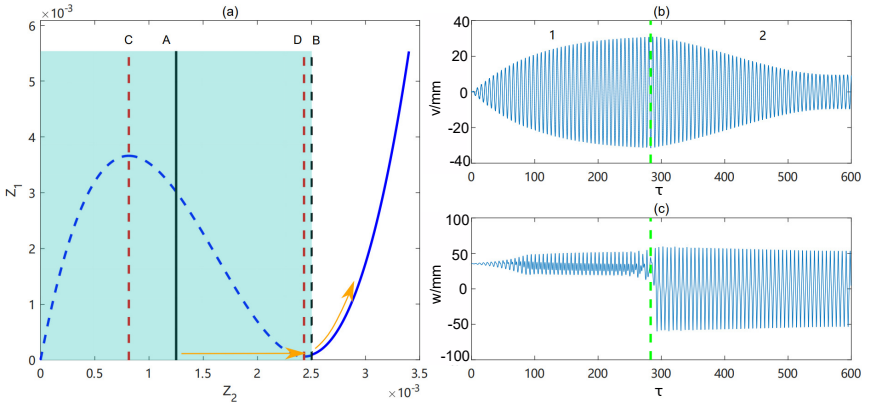

Fig. 21 Characteristic abnormal bistable global SIM and response in the time domain at harmonic excitation G = 0.65 mm, σ = 0. (a) The global SIM structure with unstable region (shaded). The orange arrow line indicates various stages in one SMR cycle. (b) displacement of w; (c) displacement of v. The green lines divide the SMR into various stages corresponding the global SIM explanation by the orange arrow line.

phase, are installed perpendicular to the conical springs like (b) in Fig. 22. The force-displacement relation of combining system can be expressed as follows:

$$\begin{aligned} F &= k_2 u + k_3 u^3 \\ k_2 &= \left(a_1 + k_0 - 2k_l \frac{l_p}{l_{0l}+2l_c-l_p}\right), k_3 = \left(a_3 + k_l \frac{l_{0l}+2l_c}{(l_{0l}+2l_c-l_p)^3}\right) \end{aligned} \tag{26}$$

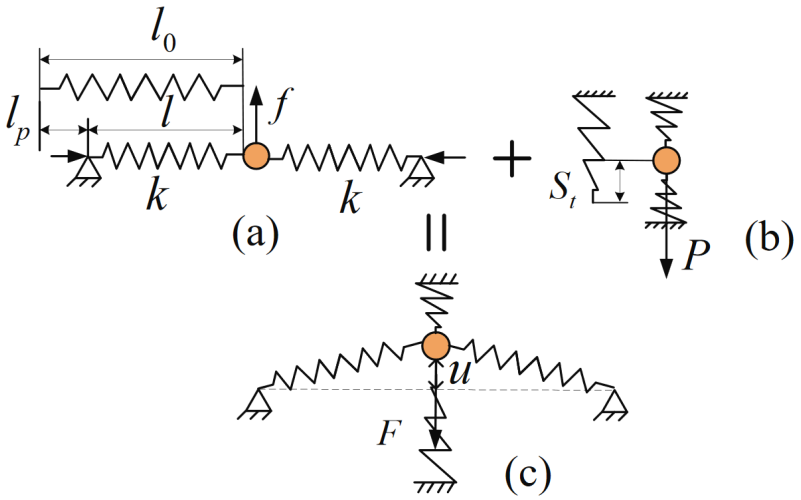

Fig. 22 Detailed diagram of the bistable NES system: (a) negative stiffness mechanism, (b) conical spring system, (c) combining system

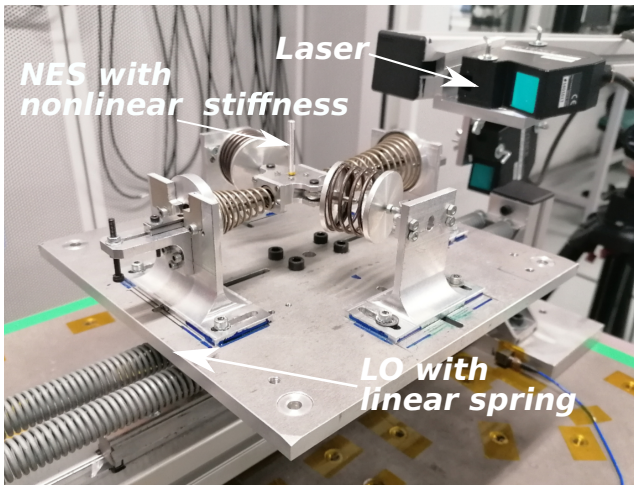

Fig. 23 Global view of the experimental setup. The four spring system constructs the nonlinear stiffness. LO is connected to a shaker by the linear spring and vibrates in a track

where k_0 represents the linear phase stiffness and a_1, a_3 are the linear stiffness and cubic nonlinearity in the nonlinear phase of a conical spring. l_{0l} and l_c are the lengths of the linear spring and connector, respectively. k_l is the stiffness of the linear spring. The pre-compression length l_p determines the value of both the negative stiffness k_3 and the nonlinear stiffness k_2. The detailed parameters and 3 initial pre-compression lengths for 3 different bistable NES cases are presented in Table. 1.

Table 1 Experimental parameters of NES system

k_0	a_1	a_3	k_l	l_{0l}
187N/m	280N/m	3.6e5N/m^3	1060N/m	50mm
	l_c	l_{p1}	l_{p2}	l_{p3}
	14.5mm	16mm	17.5mm	21mm

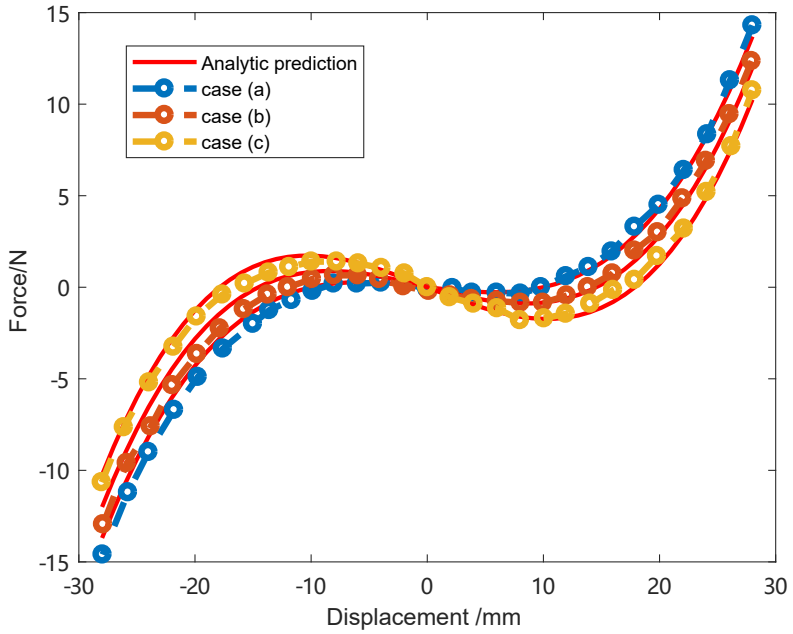

Fig. 24 Force displacement of different experiment tests with parameters in Table. 3

The corresponding static force-displacement figures for each case are presented in Fig. 24. In each case, the theoretical result provides sufficient accuracy to describe the experimental result and two equilibria (F = 0), one on either side of the displacement, which characterize a bistable NES. The distance between the equilibrium points becomes greater when the l_p increases, resulting in increased span and depth of the potential well. So it can be concluded that the control strategy of changing the length of pre-compression to produce desirable stiffness characteristics is feasible. However, increasing l_p will not only increase the value of δ but also cause an augmentation of K, which is different from the idea of purely introducing δ and keeping K constant used in the previous bistable NES classification.

The testing system consisted of a NES embedded with a LO. A 10 kN electrodynamic shaker provided the excitation at a variable frequency. The absolute displacements of NES and LO were measured by two laser systems installed vertically. The bandpass filter filtered the high-frequency noise, thus

Table 2 Experimental parameters

Physical parameters	m_1	m_2	c_1	c_2	k_1
	5.5kg	0.05kg	5 Ns/m	0.5Ns/m	1.148e4N/m
Reduced parameters	ϵ	λ_1	λ_2	f_0	
	0.91%	2.19	0.22	7.27	

Table 3 Experimental stiffness coefficients

	case (a)	case (b)	case (c)
k_3	-71.4	-136.3	-300.1
k_2	6.95e5	7.2e5	7.89e5
δ	-0.68	-1.31	-2.89
K	6.59e3e5	6.90e3	7.58e3

correcting the raw signal and the biases. The amplitude of excitation was 0.08 mm, which was the minimum value that the shaker could apply. Its frequency was varied from 7 Hz to 7.6 Hz at a sweep velocity of 0.01 Hz/s.

The mass of the NES was small, so the inertia of the springs was not negligible. The effective mass of a conical spring and a linear spring can be found in [14]. The viscous damping coefficient was estimated by modal analysis, where the nonlinear stiffness was replaced by linear stiffness. The physical parameters are summarized in Table 2. The different negative stiffnesses caused by various pre-compression lengths are presented in Table 3

Fig. 25 shows the experimentally obtained frequency response function for the small amplitude excitation G = 0.08 mm, where 3 cases perform intra-well oscillation. The analytical result was obtained by substituting the reduced parameters in Tab. 2 and 3 into (6) and resolving the amplitude of LO $|\phi_{10}|$.

When a natural frequency excitation is applied in LO, the resonance phenomenon is activated. The LO possesses the largest amplitude, of 7.23Hz, close to the predicted value of 7.26Hz. In general, the analytical method described the intra-well oscillation correctly under various δ cases as shown in Fig. 25. The analytical amplitude, which is compared with the experimental result, had the same error distribution under different negative stiffnesses. On the two sides of the natural frequency, the analytical result was usually lower than the experimental result. In the vicinity of the natural frequency, the analytical result had a higher amplitude in Fig. 25(a),(b). This error distribution is the same as the numerical test of Fig. 6(b), where the analytical method possesses a larger result near $\sigma = 0$. In the most intensive δ case in Fig. 25c, the calculation method gave a lower analytical result. This confirms the previous conclusion that the adapted complex variables method leads to minor error in the modest bistable case under small excitation. This is due to the fact that the negative stiffness value is too large to cause deformation of the real phase trajectory near the equilibrium point (which does not conform to the assumption of a circle).

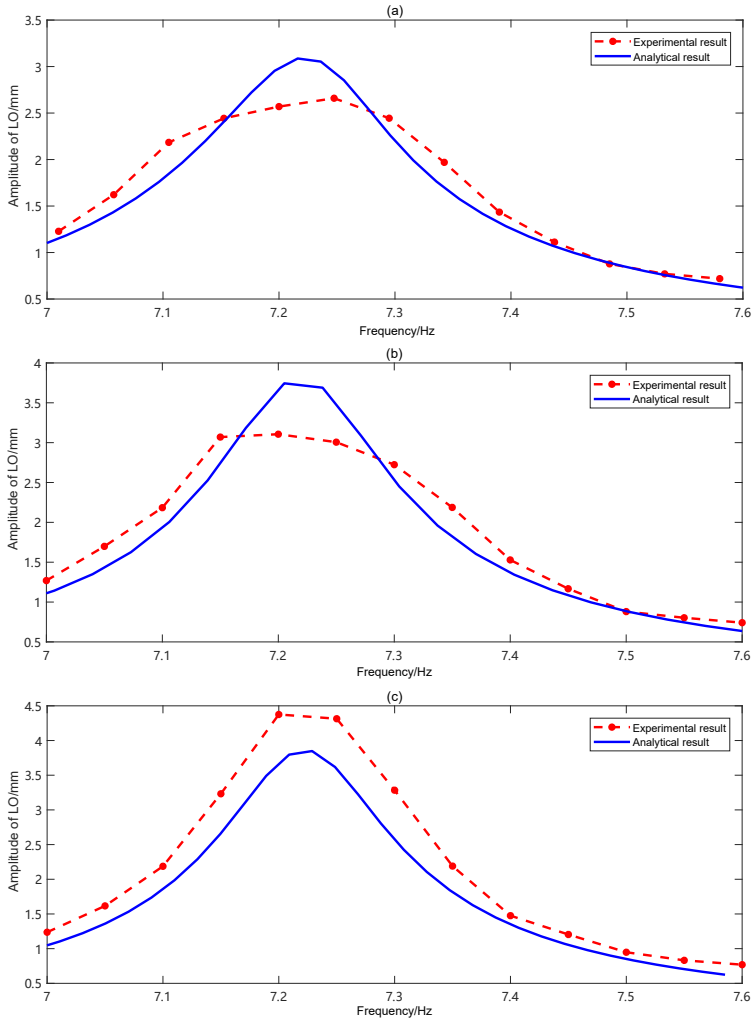

Fig. 25 Experimental and analytical frequency response curve of LO for different pre-compression length cases. The parameters of the 3 cases are presented in Table. 3

6 Response regimes in frequency domain

The previous section described the response regimes in various energy input levels. However, the advantage of a NES in absorbing energy is more apparent in the frequency domain. In this section, the response of the bistable NES is investigated experimentally over a broader range of frequencies.

The three different compression cases, having parameters that were identical to those of the previous intra-well experimental validation, were tested under a frequency sweeping excitation from 7Hz to 7.6Hz. The same frequency

sweeping process with different excitation amplitudes was repeated to record the responses of the LO and NES.

6.1 Case (a) experiment

11 sets of excitation amplitudes, from small to large values: 0.08mm, 0.10mm, 0.12mm, 0.15mm, 0.18mm, 0.21mm, 0.25mm, 0.28mm, 0.32mm, 0.36mm, and 0.4mm, were tested for case (a). To help distinguish them, the adjacent time-displacement curves are marked with different colours.

In Fig. 26, the black diamond points distinguish the SMR region and resonance peak (potential risk case), where the amplitude of the LO is enormous, and the efficiency of absorbing energy fails for the NES.

In the first case (G = 0.08mm), the stable response was the primary behavior. Intra-well oscillation appeared during the whole frequency domain. The NES oscillated around the equilibria.

In the vicinity of the natural frequency, 7.26Hz, 1: 3 subharmonic oscillation occurred first at low energy input (G = 0.1mm) and became more obvious at G = 0.12mm.

After the external excitation reached a threshold (G = 0.18mm), the region of 1: 3 subharmonic resonance broke and expanded to higher and lower frequency sides with increasing external excitation amplitude. In the neighbourhood of the natural frequency, the response reverted to a 1: 1 resonance. It also implies that the phase trajectory is re-attracted to the left branch of global SIM as case 3 in weak bistable NES simulation of Fig. 12c. In the simulation, the system returns from a chaotic motion into periodic motion with increase of excitation amplitude. In the experiment, the NES system turned from subharmonic oscillation into periodic motion. This may be because of the property of shift-frequency excitation. The 1:3 subharmonic was activated in low frequency. When the frequency of excitation was tuned to f_0, the previous 1:3 subharmonic oscillation was kept. The stability of subharmonic oscillation was better than the chaos behavior, which did not occur as predicted by the traditional analysis framework. So characteristic response of weak bistable NES (re-attraction stage) was observed.

Once G = 0.21mm was applied in case (a), SMR cycles appeared in the frequency interval [7.27Hz, 7.38Hz], which is marked by two black diamond points. The first snap-through motion and last jump-back motion of NES define the interval of SMR in Fig. 26(b). For the left boundary, at 7.27Hz, the LO always had the maximal amplitude. For the right boundary, at 7.38Hz, the LO possessed minimal local amplitude after several cycles of SMR. This indicated the effect of absorbing the energy of the SMR. The chaotic motion occupied two adjacent efficient TET, which resulted in the augmentation of LO amplitude in Fig. 26(a).

The SMR interval expanded to [7.21Hz, 7.47Hz] under greater excitation, G = 0.25mm. Then G continued to increase to 0.32mm, the interval of SMR became broader [7.15Hz, 7.47Hz]. As G increased from 0.21 to 0.32mm, the

left boundary, where SMR appeared, decreased from 7.23Hz to 7.15Hz, while the right boundary, where SMR vanished, expanded from 7.38Hz to 7.47Hz accordingly. This demonstrates a broader efficient range for performing TET for a higher energy input before the resonance peak occurs.

In G = 0.36mm, the duration of amplitude decline of SMR has extended irregularly and caused a potential risk region near the left interval boundary. Meanwhile, the frequency range of SMR has achieved the maximum of [7.13Hz, 7.54Hz]. The case (a) design has the best robustness facing the uncertainty of excitation frequency under G = 0.36mm. The 1: 3 subharmonic oscillation appeared in the low-frequency region. Then the SMR occurred in the vicinity of natural frequency. The systems returned to a stable response if frequency continued to increase.

When G = 0.4mm, the resonance peak appeared between 7.05Hz and 7.25Hz. Within the resonance interval, the LO amplitude significantly exceeded the other cases, the NES lost its ability to absorb energy, and the system was at risk. A resonance peak occurred due to the existence of three solutions in the singularity equation in the low-frequency region, one of which had a large stable amplitude. However, in the vicinity of the natural frequency, 7.26Hz, the LO had a stable minimal amplitude of 2.8mm, which represents the singularity point of the right global SIM branch. So there is a trade-off relationship between the co-existence of the best performance of NES and the worst resonance peak at the amplitude of G = 0.4mm for case (a) design. The best design also provided a possibility of worse behavior at low frequency. So the feasibility of optimal design case (a) depended on the perturbation of harmonic excitation frequency.

When the excitation increased from 0.08mm to 0.4mm, in the vicinity of natural frequency of LO, there are five stages that appeared in turn: (1) intra-well oscillation stage, (2) 1:3 subharmonic oscillation stage, (3) re-attraction stage, (4) SMR, (5) stable response. Those five stage are marked in Fig.26(b) with the green dashed boxes. Those response regimes are similar to the weak bistable NES classification based on the numerical response regimes.

6.2 Case (b) experiment

Then the pre-compression length was increased to 17.5mm, case (b) possessed larger negative stiffness $|\delta|$ and cubic nonlinearity parameters K. Similarly to case (a), the system (b) was also used with 12 sets of sweeping frequency excitations of different amplitudes: 0.08mm, 0.10mm, 0.12mm, 0.15mm, 0.18mm, 0.21mm, 0.25mm, 0.28mm, 0.32mm, 0.36mm, 0.40mm, 0.44mm. Frequency varied from 7Hz to 7.6Hz.

An essential characteristic of case (b) was the extensive range of apparent chaotic motion, which replaced the subharmonic motion of case (a). A larger depth value of potential well $\delta^2/4K$ enhanced the stability of intra-well oscillation.

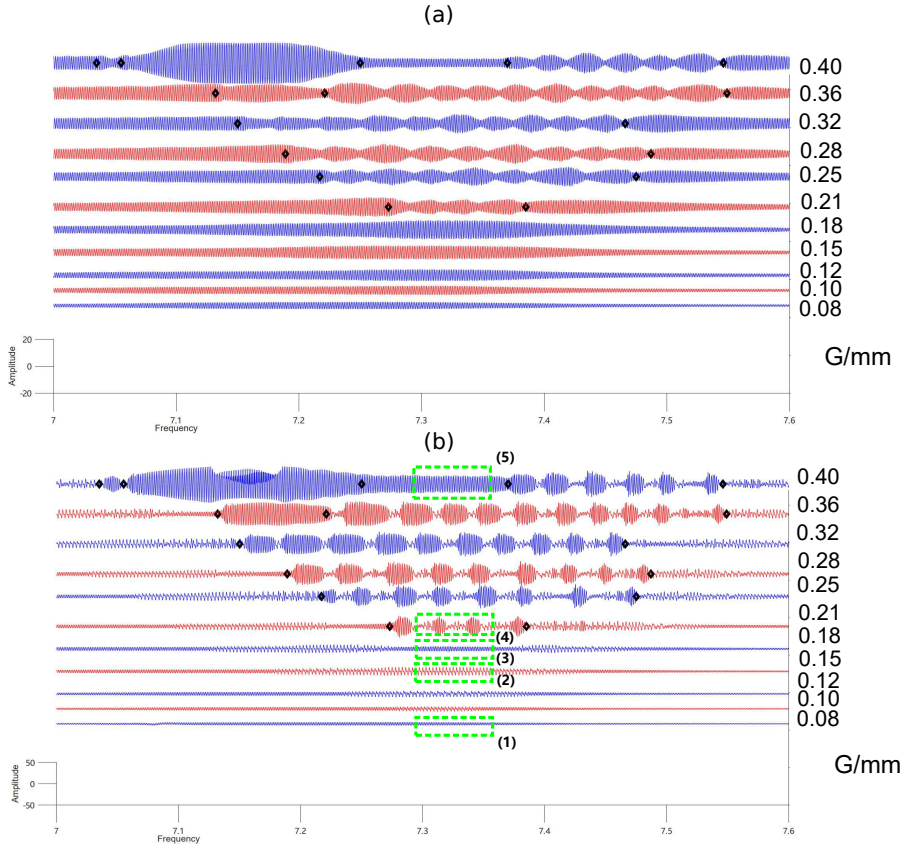

Fig. 26 (a) Frequency response of LO (b) frequency response of NES for case (a). The amplitudes of excitation are selected as 0.08mm, 0.10mm, 0.12mm, 0.15mm, 0.18mm, 0.21mm, 0.25mm, 0.28mm, 0.32mm, 0.36mm, 0.4mm. The black diamond distinguishes the SMR region from the resonance peak region. The green boxes indicate the characteristic regimes.

In the first three cases (0.08mm, 0.10mm, 0.12mm), the system oscillated in one of the wells over the frequency.

The chaos motion occurred first for G = 0.15mm. A single and weak SMR was also observed for G = 0.18mm, which is lower than the SMR occurrence threshold of case (a) (G = 0.21mm) in Fig. 27. The SMR was generated near the natural frequency and divided the chaotic region. The chaos frequency range expanded toward lower and higher frequency sides as the excitation increased.

For excitation G from 0.21mm to 0.32mm, the frequency interval for SMR occurrence expanded from a narrow range [7.29Hz, 7.31Hz] to [7.18Hz, 7.47Hz].

When G became 0.36mm, a potential resonance peak also occurred. However, the frequency range of resonance peak [7.13Hz, 7.18Hz] was narrower than that of case (a). This tendency was more obvious in the response of NES under G = 0.4mm, where the resonance peak region was [7.10Hz, 7.23Hz]. This

range was narrower than the [7.05Hz, 7.25Hz] of case (a). The resonance peak occurred when the system did not give a stable response at 7.26Hz. At the same time, the interval in which SMR occurred widened to [7.23Hz, 7.56Hz].

At the amplitude G = 0.44mm, the first signs of the steady-state response of LO at the natural frequency of 7.25Hz appeared, where the LO amplitude in Fig. 27 tended to be stable and locally minimal between the SMR and resonance peak. SMR range still dominated the extensive range [7.25Hz, 7.58Hz] and moved to a higher frequency side. An effective SMR range was also enhanced in a high energy input case. A larger compression length can reinforce the amplitude threshold required for the emergence of an optimal stable periodic response (saturation of absorbing energy).

When the excitation increased from 0.08mm to 0.44mm, in the vicinity of the natural frequency of LO, there were four stages that appeared in turn: (1) intra-well oscillation stage, (2) chaotic motion, (3) SMR, (4) stable periodic response (sign appeared). Those four stages are marked in Fig.27(b) with the green dashed boxes. The re-attraction stage disappears as a prediction of the numerical simulation: the overlap of unstable region and chaos region prevents the phase trajectory jump back to the left global SIM branch. So re-attraction motion disappeared. The characteristic of modest bistable NES: the expansion of chaotic motion was observed.

6.3 Case (c) experiment

Case (c) could be achieved by continuing to compress the pre-compression length to 21mm. Case (c) was used with the same amplitude condition as case (b), except for the 0.15mm and 0.44mm cases. The negative stiffness continued to be enhanced.

Neither chaotic motion nor subharmonic motion is observed in Fig. 28. It can be interpreted as a model of strong bistable NES that the narrow distance between trigger line B and singularity line D causes the phase trajectory to start snap-through motion and jump to the right branch of the global SIM as soon as it comes out of the well. So, before the system oscillates around the right branch of the SIM, the chaos motion is replaced by the 1:1 resonance.

This first SMR appeared at G = 0.18mm, which is the same as case (b) in Fig. 28. The frequency range of SMR increased from [7.18Hz, 7.20Hz] to [7.05Hz, 7.41Hz], as the excitation amplitude rose from 0.18mm to 0.36mm. The SMR range expanded to a lower and higher frequency sides. In case (a) and case (b), there was a significant chaotic motion between the two adjacent SMR cycles. In case (c), this chaotic phenomenon is not obvious.

The range of potential resonance peak is [7.07Hz, 7.19Hz] for G = 0.4mm. Compared with the resonance peak in case (b) for G = 0.36mm, the excitation threshold for the occurrence of resonance increased and its appearance was delayed. The resonance situation was improved. Although, the stable periodic response (optimal state) is not observed because of the limitation of the laser

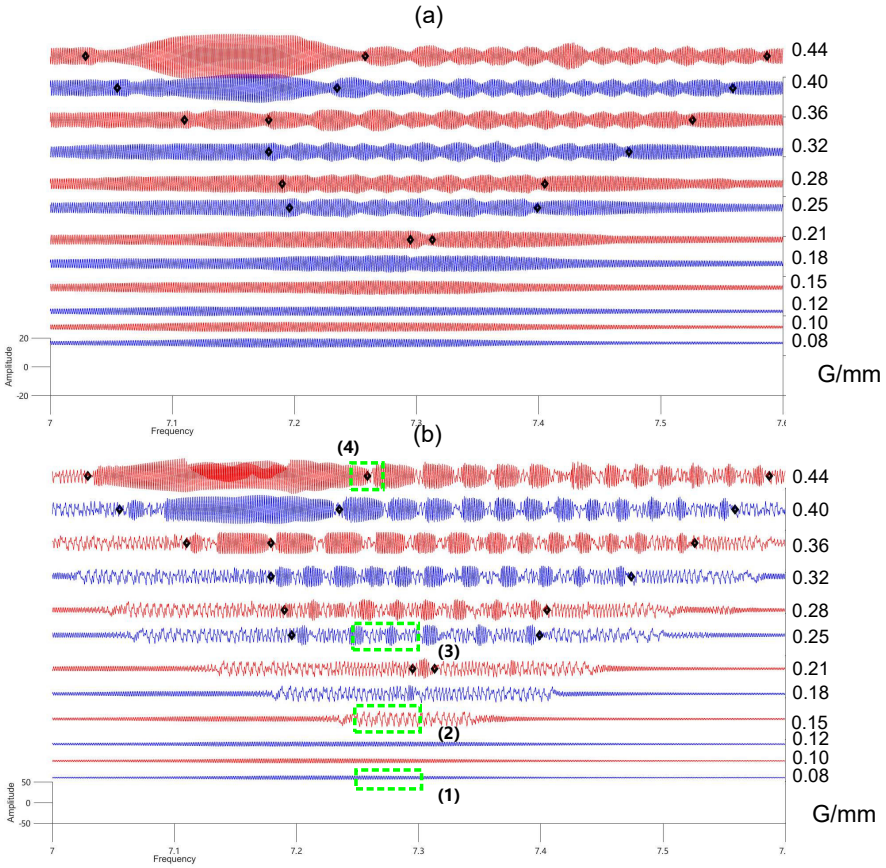

Fig. 27 (a) Frequency response of LO (b) frequency response of NES for case (b). The amplitudes of excitation are selected as 0.08mm, 0.10mm, 0.12mm, 0.15mm, 0.18mm, 0.21mm, 0.25mm, 0.28mm, 0.32mm, 0.36mm, 0.40mm, 0.44mm. The black diamond distinguishes the SMR region from the resonance peak region. The green boxes indicate the characteristic regimes.

displacement sensors. It can be inferred that his optimal state occurs above excitation amplitude of 0.4mm.

When the excitation increased from 0.08mm to 0.4mm, in the vicinity of the natural frequency of LO, there were two stages that appeared in turn: (1) intra-well oscillation stage, (2) SMR, The third stage stable response can be inferred by the numerical simulation. Those two stages are marked in Fig.28(b) with the green dashed boxes. The disappearance of chaotic motion is the characteristic symbol of a strong bistable NES.

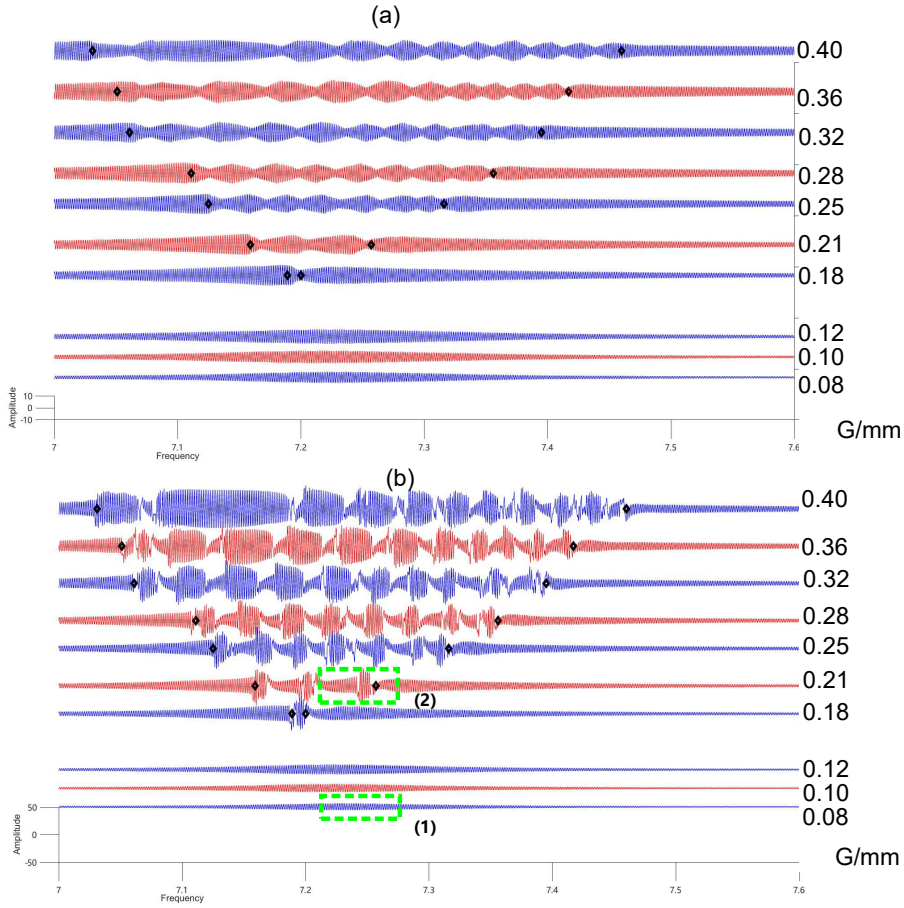

Fig. 28 (a) Frequency response of LO (b) frequency response of NES for case (c). The amplitude of excitation are selected as 0.08mm, 0.10mm, 0.12mm, 0.18mm, 0.21mm, 0.25mm, 0.28mm, 0.32mm, 0.36mm, 0.40mm. The black diamond distinguishes the SMR region and resonance peak region. The green boxes indicate the characteristic regimes.

7 Conclusions

The study focuses on the qualitative analysis of response regimes in bistable NES. Several main conclusions can be drawn:

1. The adapted complex variables method, which defines the equilibrium point as an original coordinate, performs better to approach the dynamic behaviors of intra-well oscillation. The numerical investigation reveals its natural stability of intra-well oscillation. This method gives a good fitting result and has been compared with the numerical results in the frequency domain. The actual phase trajectory of intra-well oscillates along with the constructed local Slow Invariant Manifold (SIM), which describes the low

energy behaviors better than the classic method. But the local SIM's reliability is constrained to intra-well oscillation.

2. A simplified model of triggering chaos has showed that the phase trajectory expands in a circular form with the equilibrium point as the center within the pseudo-separatrix. Despite being simple, the chosen approach enabled us to predict the analytical harmonic excitation amplitude for chaos occurrence. The numerical chaos boundary has proved the reliability of its analytical prediction in weak negative stiffness cases. The Melnikov method enables the calculation of the critical damping of the NES for triggering chaos and is validated by numerical simulations.
3. The relative position between the chaos trigger line and the global SIM structure has been proposed to illustrate the variation of the triggering Strong Modulated Response (SMR) condition. The variety in relative position of those lines enables us to explain the disappearence of response stages with larger negative stiffness value $|\delta|$ cases and for various energy levels. On the other hand, the location of chaos trigger line B in the global SIM structure classifies the bistable NES as a weak, modest, strong or abnormal bistable NES. A more efficient way to dissipate energy has been found in the modest bistable case, due to the small distance between the chaos trigger line and the singularity line in the global SIM structure.
4. The frequency-response experiment of Linear Oscillator (LO) amplitude was carried out to validate the feasibility of the adapted variables complex method. Good agreement between the theoretical and experimental results of intra-well oscillation under different negative stiffnesses was observed. Experiment confirms that the number of response regimes in the vicinity of f_0 will reduce with a more significant value of $|\delta|$, which is predicted in the numerical simulation. The design of a modest bistable NES provides the broadest frequency range of SMR for the same excitation input and helps to reduce the risk of the resonance peak in the frequency domain.

8 Compliance with Ethical Standards

Conflict of Interest: The authors declare that they have no conflict of interest.

Funding: The authors acknowledge the Chinese Scholarship Council under Grant No. 201801810128 for their financial support.

Data Availability Statements: The authors declare that the data supporting the findings of this study are available within the article.

References

1. Vakakis, A.F., Gendelman, O.V., Bergman, L.A., McFar-land, M.D., Kerschen, G., Lee, Y.S.: Nonlinear Targeted Energy Transfer in Mechanical and Structural Systems, Springer, Amsterdam (2009)
2. Vakakis, A. F., Gendelman, O.v.: Energy pumping in nonlinear mechanical oscillators: partii—resonance capture, J.Appl Mech.,68(1), 42–48(2001)

3. Gendelman, O., Manevitch, L., Vakakis, A., and M'Closkey, R.: Energy Pumping in Nonlinear Mechanical Oscillators: Part I — Dynamics of the Under-lying Hamiltonian Systems, ASME J. Appl. Mech.,68(1), pp. 34–41(2001)
4. Starosvetsky. Y., Gendelman, O.V.: Strongly modulated response in forced 2DOF oscillatory system with essential mass and potential asymmetry, Physica D: Nonlinear Phenomena, 237(13), 1719-1733(2008)
5. Starosvetsky,Y., and Gendelman,O.: Responseregimes of linear oscillator coupled to nonlinear energysink with harmonic forcing and frequency detuning, J.Sound Vib., 315(3), 746–765(2008)
6. Starosvetsky Y, Gendelman O.: Attractors of harmonically forced linear oscillator with attached nonlinear energy sink. ii: Optimization of a nonlinearvibration absorber, Nonlinear Dyn., 51(1-2), 47–57(2008)
7. Vaurigaud B, Savadkoohi A T, Lamarque C H.: Targeted energy transfer with parallel nonlinear energy sinks. part i: design theory and numericalresults, Nonlinear Dyn., 66(4), 763–780(2011).
8. McFarland D M, Kerschen G, Kowtko J J, et al.: Experimental investigation of targeted energy transfers instrongly and nonlinearly coupled oscillators, J. Acoust. Soc. Am., 118(2), 791–799(2005)
9. Bellet R, Cochelin B, Herzog P, et al.: Experimental study of targeted energy transferfrom an acoustic system to a nonlinear membrane absorber, J.Sound Vib., 329(14), 2768–2791(2020)
10. AL-Shudeifat M A.: Nonlinear energy sinks with piecewise-linear nonlinearities, Int.J Non Linear Mech, 14(12),124501(2019)
11. Saeed A S, AL-Shudeifat M A, Vakakis A F.: Rotary-oscillatory nonlinear energy sink of robust performanc, Int.J Non Linear. Mech, 117, 103249(2019)
12. Li T, Gourc E, Seguy S, et al.: Dynamics of two vibro-impact nonlinear energy sinks in parallel under periodic and transient excitations. Int.J Non Linear. Mech, 90, 100-110(2017)
13. D. Qiu, S. Seguy, M. Paredes.: Design criteria for optimally tuned vibro-impact nonlinear energy sink, J. Sound Vib, 442, 497-513(2019).
14. Qiu D, Seguy S, Paredes M.: Tuned nonlinear energy sink with conical spring: design theory and sensitivity analysis, J.Mech.Design, 140(1), 011404(2018)
15. Al-Shudeifat, Mohammad A.: Highly efficient nonlinear energy sink. Nonlinear Dyn, 76(4), 1905-1920(2014)
16. Al-Shudeifat M A, Wierschem N, Quinn D D, et al.: Numerical and experimental investigation of a highly effective single-sided vibro-impact non-linear energy sink for shock mitigation. Int J Non Linear Mech, 52, 96-109(2013).
17. Chen Y Y, Qian Z C, Zhao W, et al., A magnetic bi-stable nonlinear energysink for structural seismic control, J. Sound Vib.,473,115233(2020)
18. Gourc E, Seguy S, Michon G, et al.: Quenching chatter instability in turning process with a vibro-impact nonlinear energy sink, J.Sound Vib., 355, 392-406(2015)
19. Manevitch L I.: The description of localized normal modes in a chain of nonlinear coupled oscillators using complex variables. Nonlinear Dyn, 25(1),95-109(2001)
20. Manevitch L I, Sigalov G, Romeo F, et al.: Dynamics of a linear oscillator coupled to a bistable light attachment: analytical study, J. Appl. Mech., 81(4), 041011(2014)
21. Romeo F, Sigalov G, Bergman L A, et al.: Dynamics of a linear oscillator coupled to a bistable light attachment: numerical study, J. Comput. Nonlinear. Dynam, 10(1), 011007(2015)
22. Bitar D, Savadkoohi A T, Lamarque C H, et al.: Extended complexification method to study nonlinear passive control. Nonlinear Dyn, 99(2), 1433-1450(2020).
23. Qiu D, Li T, Seguy S, et al.: Efficient targeted energy transfer of bistable nonlinear energy sink: application to optimal design, Nonlinear Dyn, 92(2), 443-461(2018)
24. D. Qiu, M. Paredes, S. Seguy.: Variable pitch spring for nonlinear energy sink: application to passive vibration control, Proc Inst Mech Eng C J Mech Eng Sci, 233, 611-622(2019).
25. Z. Wu, S. Seguy, M. Paredes.: Basic Constraints for Design Optimization of Cubic and Bistable NES[J]. J. Vib. Acoust, 144, 1-51(2021).

26. Fang X, Wen J, Yin J, et al.: Highly efficient continuous bistable nonlinear energy sink composed of a cantilever beam with partial constrained layer damping, Nonlinear Dyn, 87(4), 2677-2695(2017)
27. Benacchio S, Malher A, Boisson J, et al.: Design of a magnetic vibration absorber with tunable stiffnesses, Nonlinear Dyn, 85(2), 893-911(2016)
28. Pennisi G, Mann B P, Naclerio N, et al.: Design and experimental study of a nonlinear energy sink coupled to an electromagnetic energy harvester, J.Sound Vib, 437, 340-357(2018)
29. Pirrera A, Avitabile D, Weaver P M.: Bistable plates for morphing structures: a refined analytical approach with high-order polynomials, Int J.Solids Struct, 47(25-26), 3412-3425(2010)
30. Johnson D R, Thota M, Semperlotti F, et al. On achieving high and adaptable damping via a bistable oscillator, Smart Mater Struct, 22(11), 115027(2013)
31. Iurasov V, Mattei P O.: Bistable nonlinear damper based on a buckled beam configuration, Nonlinear Dyn, 99(3), 1801-1822(2020)
32. Romeo F, Manevitch L I, Bergman L A, et al.: Transient and chaotic low-energy transfers in a system with bistable nonlinearity, Chaos, 25(5), 053109(2015)
33. Dekemele K, Van Torre P, Loccufier M.: Performance and tuning of a chaotic bi-stable NES to mitigate transient vibrations, Nonlinear Dyn, 98(3), 1831-1851(2019)
34. Farshidianfar A, Saghafi A.: Global bifurcation and chaos analysis in nonlinear vibration of spur gear systems, Nonlinear Dyn, 75(4), 783-806(2014)
35. Wolf, A., Swift, J.B., Swinney, H.L., Vastano, J.A.: Determining lyapunov exponents from a time series. Physica D 16(3), 285–317 (1985)
36. Govorukhin, V.: Calculation lyapunov exponents for ode. https://nl.mathworks.com/matlabcentral/fileexchange/4628-calculation-lyapunov-exponents-for-ode (2004)